Coupled Modeling of Flow, Surface Chemistry and Material Response

Erin Farbar, Abhilasha Anna and Iain D. Boyd
Department of Aerospace Engineering
University of Michigan
Ann Arbor, Michigan, USA
iainboyd@umich.edu

ABSTRACT

Physically accurate predictions of the response of Thermal Protection Systems to the evolution of the surrounding hypersonic flow field requires a coupled computational approach in which the influence of the surface processes and the response of the material on the flow field evolution is considered. In this article, details of each of the flow, surface, and material models that form the components of this coupled, computational framework are presented. An approach to coupling the three components, motivated by the large separation of the associated characteristic time scales, is presented. Examples of analyses are then provided that illustrate the application of the coupled framework to the simulation of both an Inductively Coupled Plasma Torch experiment and a hypersonic flight vehicle, involving a range of flow and and surface conditions.

1.0 INTRODUCTION

The Thermal Protection System (TPS) provides insulation for an atmospheric entry probe or vehicle from the severe aerodynamic heat load encountered during hypersonic flight through a planetary atmosphere. It is a single point of failure system as the prolonged exposure to high temperature can cause the TPS materials to fail. Depending on the heat load encountered during hypersonic flight, an ablative or non-ablative TPS may be used. Non-ablative or reusable materials (for example, the ceramic tiles used on the Space Shuttle) are used where the re-entry conditions are relatively mild. Ablative materials are used where relatively high heating rates are generated during flight (for example, the Apollo, Mars Viking and Pioneer Venus missions). Figure 1 shows examples of the mission trajectories and conditions suitable for non-ablative (reusable) and ablative TPS to be used effectively. It is evident from this Figure that future missions involving entry into the atmospheres of other planetary bodies, or re-entry to Earth, will utilize some form of ablative TPS.

The choice of a TPS material is determined by its ability to withstand the anticipated aerothermal environment for a specific mission. Peak heat flux is the deciding factor in selecting the TPS material that will sustain the desired level of heating. However, integrated heat load is the key factor in determining the required thickness of the TPS [2]. The desire to reduce TPS mass fraction, and therefore increase payload mass fraction, drives the need to produce accurate predictions of the heat flux to the TPS structure throughout a mission trajectory. This is accomplished through ground or flight testing and computational modeling, and the topic of the latter is addressed in this article.

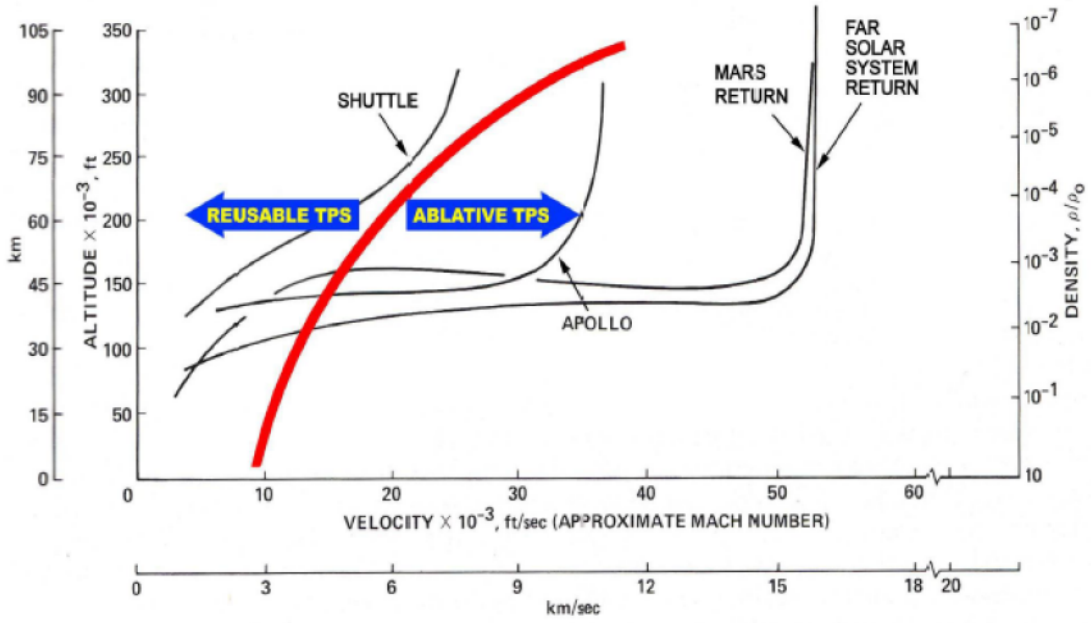

Figure 1: Conditions for reusable and ablative TPS [1]

Experimental testing is expensive, and no single high enthalpy ground test facility can recreate all flight conditions simultaneously. Thus, Computational Fluid Dynamics (CFD) is an important tool for TPS testing, design and development. Additionally, CFD simulations can be used in identifying test article failures and optimized testing conditions. When a CFD code is coupled with a material response code and a model to describe the interaction of the gas flow with the TPS material, CFD becomes an important tool in the vehicle TPS design and sizing assessment. Figure 2 shows the physical processes that take place in each component of the gas-surface-material system, and the method by which these physical processes are modeled. In the gas flow component, the formation of strong shocks, thermochemical nonequilibrium, and the properties of the boundary layer are modeled using CFD. Physical modeling information must be supplied to the CFD code, such as the relaxation times for internal energy modes, and rate coefficients for finite-rate chemical reactions. In the TPS material component, the conduction of heat through the material, pyrolysis, and the flow of gas through the porous material are modeled using a material response code. In this article, the behavior of non-charring ablative TPS materials is addressed, so pyrolysis and gas flow within the solid material are not considered. The physical properties of the complex material, such as conductivity and tortuosity, must be supplied to the material response code. The surface component provides the interface by which the gas flow and TPS material interact. Physical processes that take place on the surface include accommodation, oxidation, sublimation, and catalysis. These processes are modeling using a finite-rate surface chemistry (FRSC) module. The mechanisms of surface interactions and their associated rate coefficients must be supplied to the FRSC module.

Progress towards consistent coupling of each of the individual component models of gas flow, surface, and TPS material is the topic of this article. Section 2 provides the details of each of the flow, surface, and material component modules. Section 3 describes, in detail, how these modules are coupled to produce a computational tool capable of consistently simulating all aspects of the flow-surface-material system. Section 4 presents two

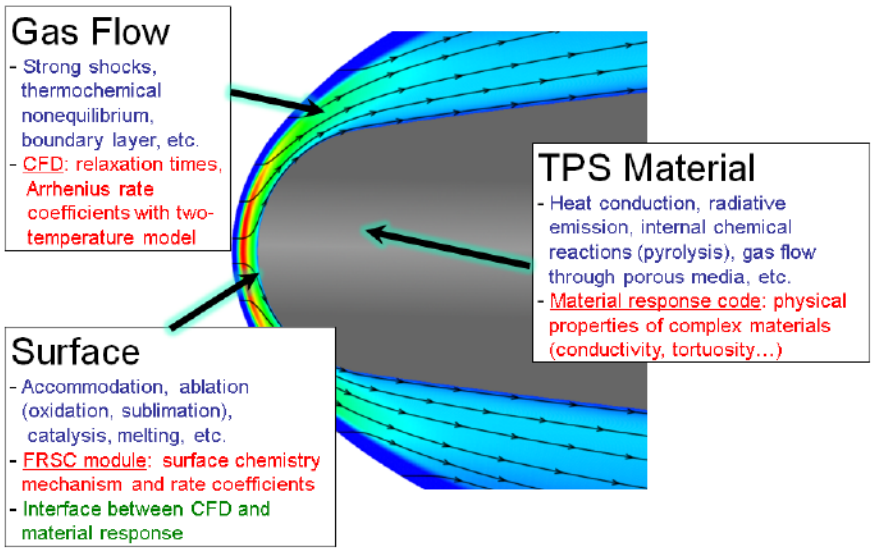

Figure 2: Components of the coupled computational framework.

examples of the application of this coupled code. The partial validation of this approach using data from an Inductively Coupled Plasma Torch (ICP) facility is described in detail, and it is demonstrated that including the material response in the coupled simulation results in better agreement with the experimental data. An example of the application of the coupled code to the simulation of a hypersonic flight vehicle is also presented, and the choice of surface chemistry mechanisms is shown to have a significant effect on the predicted surface properties. Finally, Section 5 presents a summary of the article.

2.0 COMPONENT MODULES FOR COUPLED MODELING

2.1 Nonequilibrium gas flow

The properties of the nonequilibrium gas flow are obtained by solving the Navier-Stokes equations using a CFD code called LeMANS, which is developed at the University of Michigan [3, 4]. LeMANS is a three-dimensional, parallel code that solves the Navier-Stokes equations on unstructured meshes. In this work, it is assumed that the translational and rotational energy modes can be described by a single temperature, and that the vibrational, electronic and electron translational energy modes are described by a different temperature. The mixture transport properties are calculated using Wilke's semi-empirical mixing rule [5]. The species viscosities are calculated using Blottner's model [6] and the species thermal conductivities are calculated using Eucken's relation [7]. In this study, the Lewis number is constant with a value of 1.4. The mass diffusion fluxes are modeled using a modified version of Fick's law [8], which enforces the requirement that the fluxes sum to zero, and the diffusion flux of electrons is calculated assuming ambipolar diffusion.

A second order spatially accurate finite-volume method is used to solve the set of differential equations on unstructured meshes. LeMANS can simulate two dimensional and axisymmetric flows using any mixture of quadrilateral and triangular mesh cells, and three-dimensional flows using any mixture or hexahedra, prisms, tetrahedra and pyramids. The inviscid fluxes are discretized using a modified Steger-Warming Flux Vector Splitting approach which has low dissipation and is appropriate to calculate boundary layers [9]. The viscous fluxes

are calculated using cell-centered and nodal values. The viscous stresses are modeled assuming a Newtonian fluid and Stokes' hypothesis, and the heat fluxes are calculated according to Fourier's Law for all temperatures. A point or line implicit method is used to perform the time integration, and the code is parallelized using Metis [10] to partition the mesh, and the Message Passing Interface (MPI) to communicate information between processors.

In order to use LeMANS in coupled flow-material simulations, mesh movement capabilities have been implemented to model surface recession of ablating materials. Given the displacement of each node on the surface of the material, each node on the associated perpendicular line extending from the surface to the inflow boundary is moved along the line a distance proportional to the initial distance of the node in question from the surface node. This method of moving the mesh exploits the relatively simple, convex shape of hypersonic flight vehicles. Once the new mesh is created, the flow field quantities from the previous iteration are simply moved to the new mesh.

2.2 Surface interactions

The most general way of modeling the interaction of a gas flow with a surface is through the specification of finite-rate reaction mechanisms and the associated rates at the surface boundary. Another approach used to model an air-carbon interface is to make the assumption that the gas at the surface is in a saturated equilibrium state with the carbon surface. When combined with an assumption that the heat and mass transfer coefficients are equal at the surface, this approach results in a unique gas composition, enthalpy and mass ablation rate at each surface temperature and pressure. Thus, tables can be generated for these quantities as a function of surface temperature and pressure, and the required boundary values for the CFD calculation can be interpolated from them during the CFD simulation process. These are the so-called B_c' tables. The former approach, involving modeling finite rate chemical reactions, is presented in this article.

2.2.1 Finite-rate surface chemistry

The FRSC module developed by Marschall and MacLean [11, 12] is tightly coupled to the LeMANS CFD code. The FRSC module allows the specification of surface reactions involving both adsorbed surface species and bulk material species. These reactions are governed by sets of active sites, and by types of bulk species. Given the conditions at the vehicle surface from the CFD code, the module computes the species production rates due to surface reactions. These values are then communicated to the CFD code. The module also has the capability to model the blowing of pyrolysis gases from the surface, however this capability is not used in the present work because the behaviour of a non-charring carbon ablator is investigated. The coupling of the FRSC module to the LeMANS CFD code has been verified [13].

The FRSC Module allows for the definition of three distinct environments: gas, surface, and bulk. The surface and bulk environments can have any number of phases, which represent physically and chemically distinct regions. The gas environment can only have a single phase. Surface reactions may only occur at active sites that can either be empty or filled with an adsorbed species on a specific surface phase. The total number of reaction sites is conserved and sites may neither be created nor destroyed. The number of reaction sites (i.e. site density) is a property of the surface and is defined as a user input. The FRSC Module allows the specification of several different reaction types. These include,

Adsorption/Desorption:	A + (s) $\rightleftharpoons$ A(s)
Eley-Rideal:	A + B(s) $\rightleftharpoons$ AB + (s)
Langmuir-Hinshelwood:	A(s) + B(s) $\rightleftharpoons$ AB + (s)
Sublimation/Condensation:	(s) + A(b) $\rightleftharpoons$ A + (s)

In the previous examples, (s) represents an empty active site, A(s) is an adsorbed particle, and A(b) is a bulk species. The FRSC Module also allows for the specification of several other reaction processes that do not strictly fit into the categories given above (e.g. oxidation and nitridation).

The general form for reaction i can be expressed as,

$$\sum_{k=1}^{K} \nu'_{ki} A_k \rightleftharpoons \sum_{k=1}^{K} \nu''_{ki} A_k \tag{1}$$

where ν'_{ki} and ν''_{ki} are the stoichiometric coefficients for species k on the reactant and product sides, respectively. The net production rate for species k from all N_R surface reactions is,

$$\dot{w}_k = \sum_{i}^{N_R} \dot{w}_{ki} \tag{2}$$

where the reaction-specific production rate, $\dot{w}_{ki}$, is given by,

$$\dot{w}_{ki} = \left(\nu''_{ki} - \nu'_{ki}\right) \left(k_{fi} \prod_{k=1}^{K} X_k^{\nu'_{ki}} - k_{bi} \prod_{k=1}^{K} X_k^{\nu''_{ki}} \right) \tag{3}$$

where k_{f_i} and k_{b_i} are the forward and backward rates for reaction i, respectively, X_k is the concentration of species k at the surface, and K is the number of species considered in the surface system.

The forward reaction rates for surface processes are specified using kinetics-based formulations for specific reaction types as,

Adsorption:

$$k_f = \left[\frac{\bar{v}_A}{4\phi_s^{\nu_s}} \right] S_0 \exp\left(-\frac{E_{ad}}{RuT} \right) \tag{4}$$

Eley-Rideal:

$$k_f = \left[\frac{\bar{v}_A}{4\phi_s^{\nu_s}} \right] \gamma_0 \exp\left(-\frac{E_{ER}}{RuT} \right) \tag{5}$$

Langmuir-Hinshelwood:

$$k_f = \left[\bar{v}_{2D,A} \sqrt{Av} \right] \phi_s^{1.5-\nu_s} C_{LH} \exp\left(-\frac{E_{LH}}{RuT} \right) \tag{6}$$

Sublimation:

$$k_f = \left[\frac{\bar{v}_A}{4\phi_s^{\nu_s} RuT} \right] \gamma_{sub} \exp\left(-\frac{E_{sub}}{RuT} \right) \tag{7}$$

In these equations, the parameters $E_{ad}, E_{ER}, E_{LH}, E_{sub}$ are the energy barriers for each type of reaction mechanism. The reaction efficiency, γ_0, is defined as the ratio of the flux of atoms at the surface that react to the total flux of atoms impinging on the surface. The sticking or adsorption coefficient, S_0, is the fraction of gas-phase species that hit the surface and become adsorbed. The active site density on the surface is given by ϕ_s, M_A

is the molar weight of species A, γ_{sub} is a dimensionless evaporation coefficient, and C_{LH} is a dimensionless constant. The thermal velocities used in the rate expressions are given by,

$$\bar{v}_A = \sqrt{\frac{8RuT}{\pi M_A}} \tag{8}$$

and

$$\bar{v}_{2D,A} = \sqrt{\frac{\pi RuT}{2M_A}} \tag{9}$$

The temperature used in these expressions is the translational temperature of the gas at the surface, which is equal to the wall temperature for this work. This approach of defining the forward reaction rates is more insightful than using Arrhenius-type expressions since the Arrhenius reaction parameters may be difficult to relate to physical, chemical, or kinetic processes. Note, however, that the FRSC Module also allows for Arrhenius-type formulations for the forward rates.

The backward rate for reaction i is determined based on the forward rates and the concentration-based equilibrium constant by,

$$k_{b,i} = \frac{k_{f,i}}{K_{c,i}} \tag{10}$$

The concentration-based equilibrium constant is related to the activity-based equilibrium constant by,

$$K_{c,i} = K_{a,i} \left(\frac{P_{ref}}{RuT} \right)^{\nu_{g,i}} \tag{11}$$

where P_{ref} is a reference pressure of 10^5 Pa, which is the same value used in the NASA Glenn thermodynamic database [14], and $\nu_{g,i}$ is the net stoichiometric exponent for gas species equal to $\sum (\nu''_{ki} - \nu'_{ki})$. The activity-based equilibrium constant is related to changes in the Gibbs energy of formation and can be calculated directly if the necessary thermodynamic properties are available by,

$$K_{a,i} = \exp \left[-\frac{\Delta G_i^0(T)}{RuT} \right] \tag{12}$$

where the change in Gibbs energy of formation, $\Delta G_i^0(T)$, can be obtained from databases, such as the NASA Glenn thermodynamic database [14]. However, the difference between the Gibbs energy of formation of an occupied active site and an empty active site may not be available for most species. For these cases, either the backward rate $k_{b,i}$ or the concentration-based equilibrium constant $K_{c,i}$ must be specified in addition to the forward rate for each adsorption reaction based on statistical thermodynamics and/or kinetic theory. Then, the missing thermodynamic data for occupied and empty active sites can be calculated using Equations 11 and 12. The calculated change in Gibbs energy of formation can then be used with the available thermodynamic data for gas and solid phase species to calculate the constants for all other surface reactions. Additional details regarding the FRSC Module are provided in Ref. [11].

2.3 Material response

In this work, either a one-dimensional (MOPAR) or two-dimensional (MOPAR2) material response model is used. The MOPAR module, developed by Martin and Boyd [15, 16], uses the one-dimensional control volume

finite-element method (CVFEM) [17, 18] to model heat conduction and pyrolysis gas behaviour. The MOPAR2 module, developed by Wiebenga and Boyd [19], also uses the control-volume finite-element method to model conduction behaviour, and includes the capability to model momentum transfer within the solid. MOPAR2 has been verified using the Method of Manufactured Solutions [20].

For the examples presented in this article, either the MOPAR or MOPAR2 material response code is used to solve the energy equation in the material, which is shown in Equation 13. This Equation includes a convection term due to grid motion to allow for the material mesh to recede when surface ablation is occurring,

$$\rho\frac{\partial e}{\partial t} - \rho h(\nabla \cdot \mathbf{v_{cs}}) + \nabla \cdot \mathbf{q} = \dot{Q} \tag{13}$$

In Equation 13, e is the specific energy of the material, h is the specific enthalpy, $\mathbf{v_{cs}}$ is the velocity vector associated with the recessing surface, $\mathbf{q}$ is the heat flux vector, and $\dot{Q}$ is the material response source term.

Equation 13 is solved implicitly in both MOPAR and MOPAR2. When this equation is solved in MOPAR2, a tensor formulation of Fourier's Law is used to allow for simulation of anisotropic materials. The CVFEM method is used with linear triangular elements is used for spatial discretization. In this formulation, all variables are assumed to vary linearly across an element, which leads to a scheme that is spatially second order. The Backward Euler method is used for implicit time integration, which leads to a first order accurate discretization in time. The control surface velocity is determined from the change in node positions during a time step as the mesh is deformed.

Several different boundary conditions for Equation 13 are implemented including specified temperature, specified heat flux, re-radiation, aerodynamic heating, and thermochemical ablation. For the examples presented in this work, the information exchanged between the flow and surface modules and the MOPAR/MOPAR2 module is described in Section 3.2.

3.0 APPROACH TO COUPLING

For hypersonic entry vehicles, the time scales of the trajectories are on the order of minutes. In contrast, the nonequilibrium reactions that take place in the flow fields around these types of vehicles, and at the surface of these vehicles, have time scales that are on the order of microseconds (10^{-6} sec). Lastly, the process of conducting energy through the TPS material takes place with a time scale that is on the order of seconds.

The approach to coupling the three component modules is based on exploiting the large differences between each of these timescales. Since the chemical reactions occurring in the gas phase and on the surface are so much faster than the process of energy conduction into the material, it is reasonable to assume that the flow field and surface processes respond instantaneously to the changes in the material properties. This means that the entry trajectory, or exposure time in the case of an ablation experiment, can be discretized in time. The general approach is to treat the material response in a time-dependent fashion, and integrate Equation 13 between discrete trajectory/exposure points using information obtained from steady-state flow and surface chemistry simulations as boundary conditions. This approach is described in detail in the sections that follow.

3.1 Implementation of Surface Chemistry Coupling

The FRSC module is coupled to the CFD module through the mass balance and momentum balance equations written at the surface of the vehicle. The control volume enclosing the surface of the vehicle is drawn in Figure 3, where the terms appearing in the mass conservation equation are labeled. Using Figure 3, the mass

conservation equation can be written at the surface for each species,

$$-\rho_w D_k \frac{\partial Y_k}{\partial n}|_w + \rho_w v_w Y_{k,w} = M_k \dot{w}_k \tag{14}$$

In Equation 14, ρ_w is the density of the gas phase at the surface, D_k is the diffusion coefficient for gas phase species k, Y_k is the mass fraction of gas phase species k, and v_w is the gas phase velocity, which is assumed to be in the surface-normal direction. Equation 14 is coupled to the expression for the mass flux of bulk species at the surface ($\dot{m}_b$) by the following relation,

$$\dot{m}_b = -\sum_{k=1}^{N_{nb}} M_k \dot{w}_k = \rho_w v_w \tag{15}$$

In Equation 15, the mass flux between the bulk and the gas environment due to surface reactions is computed by summing the mass production rates of N_{nb} bulk species. In an air-carbon system, this expression contains a single term for the production rate of solid carbon, $\dot{w}_C$, which will be negative if the surface is ablating (mass is being transfered from the bulk to the gas phase).

The boundary conditions at the surface of the vehicle are determined at each iteration of the CFD solver as follows. The production rates of each gas, surface and bulk-phase species, $\dot{w}_k$, at the current iteration are calculated by the FRSC module using the values of ρ_w, $Y_{w,k}$ and T_w from the previous iteration. The production rates of the gas-phase species needed for the solution of Equation 14 are then known. The mass flux of the bulk-phase species, and thus the product $\rho_w v_w$, is then computed in LeMANS using the production rates of the bulk-phase species and Equation 15. The value of $\rho_w v_w$ is then substituted into Equation 14, and the system of N_s equations represented by Equation 14 is solved iteratively, together with the expression of momentum conservation at the surface,

$$p_n + \rho_n v_n^2 = p_w + \rho_w v_w^2 \tag{16}$$

using Newton's method in order to obtain the species mass fractions and gas-phase density required to set the boundary conditions at the wall. In Equation 16, the subscript "n" refers to a value in the first CFD cell lying along the material surface boundary, and "w" refers to a value at the surface face.

Since the system of equations is over-specified, the equation corresponding to the largest mass fraction is removed from the system prior to the solution process. The ideal gas law is used to eliminate the wall pressure, p_w, in Equation 16, and the temperature at the wall is known at the current iteration from the material response module. All of the primitive quantities at each cell-face that defines the surface of the vehicle are determined in this fashion at each iteration of the CFD solver, and the values of the conserved variables in the ghost cells are then calculated using these quantities in order to produce the required inviscid and viscous fluxes across the cell faces. Lastly, the concentrations of the surface species are updated at every iteration using a discrete form of Equation 17,

$$\frac{\partial X_k}{\partial t} = \dot{w}_k \tag{17}$$

where the time step used is the same simulation time step used in the CFD module.

3.2 Implementation of Material Response Coupling

The MOPAR module is loosely coupled to the LeMANS and the FRSC modules through the solution of the energy conservation equation at each cell face that defines the surface of the vehicle, as well as the calculated

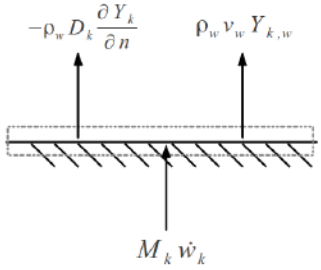

Figure 3: Control volume for species mass conservation at the surface of the vehicle.

recession rate of the vehicle's surface. The temperature of the gas at the surface is assumed to be equal to the temperature of the solid surface, and all internal energy modes of the gas-phase are assumed to be in equilibrium. The energy conservation equation at the surface of the vehicle is written using the control volume enclosing the surface of the vehicle that is shown in Figure 4.

$$q_{conv} + \dot{m}_b h_{b,w} + q_{rad} = \sigma\epsilon\left(T_w^4 - T_\infty^4\right) + \dot{m}_b h_w + q_{cond} \tag{18}$$

In Equation 18, $h_{b,w}$ is the enthalpy of the bulk phase at the surface, and h_w is the enthalpy of the gas phase at the surface. The terms on the left-hand side represent energy entering the control volume shown in Figure 4, and the terms on the right-hand side represent energy leaving the control volume at the surface. The term labeled q_{conv} is the heat flux at the surface predicted by the CFD code, which is given by Equation 19,

$$q_{conv} = \kappa_{tr}\frac{\partial T_{tr}}{\partial n}|_w + \kappa_{ve}\frac{\partial T_{ve}}{\partial n}|_w + \sum_{k=1}^{N_s}\rho D_k h_k \frac{\partial Y_k}{\partial n}|_w \tag{19}$$

In Equation 19, κ_{tr} is the conductivity of the translational-rotational energy mode, and κ_{ve} is the conductivity of the vibrational-electronic-electron translational energy mode. The term q_{cond} is the magnitude of the heat flux directed away from the surface and conducted into the solid that is predicted by the material response code. The radiative energy absorbed by the surface from the surroundings, q_{rad}, is neglected in this work. The energy radiated away from the surface, $\sigma\epsilon\left(T_w^4 - T_\infty^4\right)$, is computed in MOPAR, with T_∞ equal to the freestream temperature.

The recession rate at the surface of the vehicle is calculated as follows,

$$\dot{s}' = \frac{\dot{m}_b}{\rho_b} \tag{20}$$

where ρ_b is the mass density of the bulk material. The values of $\dot{s}'$ and $(q_{conv} + \dot{m}_b(h_{b,w} - h_w))$ at each surface face are used to provide the boundary conditions at the material-gas interface for the solution of Equation 13.

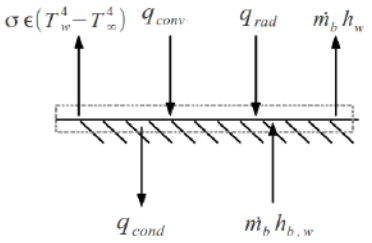

Figure 4: Control volume for energy conservation at the surface of the vehicle.

3.3 Coupling Algorithm

The coupling between the CFD and FRSC modules and MOPAR/MOPAR2 proceeds as follows. The trajectory of the vehicle or the sample exposure time is discretized into several points. A steady state flow solution is then found at each trajectory point using the solution from the previous trajectory point as the initial condition. As the CFD-FRSC solution of the flow field is marched to steady state, the material response subroutine is called after every N flow field iterations, where N is a fixed number selected before running the simulation. The value of N=200 is used for both examples presented in this article. The following input parameters are passed to MOPAR/MOPAR2:

$$Q = \theta\left(q_{conv} + \dot{m}_b\left(h_{b,w} - h_w\right)\right) + (1-\theta)Q_{prev} \tag{21}$$

$$\dot{s} = \theta\dot{s}' + (1-\theta)\dot{s}_{prev} \tag{22}$$

In Equation 21, a subscript of "prev" is used to denote values of parameters from the previous call to MOPAR or MOPAR2. The parameter θ is a damping factor that can have a value between 0 and 1; a value of 0.5 or 1.0 is used to generate all of the results presented here.

MOPAR/MOPAR2 is then used to model the material response in a time-accurate fashion between the current trajectory point (at t^n) and the previous trajectory point (at t^{n-1}). During this process, the applied heat flux is linearly interpolated between the values obtained from the converged, coupled solution at the previous trajectory point, and those from the current state of the coupled solution. The recession rate is piece-wise constant between trajectory points. Once the surface temperature, T_w', corresponding to the current state of the CFD-FRSC solution is determined, it is also damped as follows:

$$T_w = \theta T_w' + (1-\theta)T_{w,prev} \tag{23}$$

The surface temperature is used in the FRSC module to determine the production rate of each species, and to set the boundary conditions for the conservation equations in the gas-phase for the next N=200 iterations of the coupled CFD and FRSC modules.

The distance each surface face moves in the time between subsequent trajectory points is calculated as follows:

$$X_w = \dot{s}\left(t^n - t^{n-1}\right) \tag{24}$$

The displacement of each node on the surface is then formed as an average of adjacent face-centered values of X_w. The movement of every node on each line of the CFD mesh that extends from the surface is then determined such that the movement of each node is proportional to the original distance of the node from the associated surface node. This coupling process is repeated until the flow field residuals have converged.

The entire coupling strategy is represented schematically in Figure 5. In Figure 5, the surface pressure, P_w that is communicated between LeMANS and MOPAR/MOPAR2 is only used if a charring ablator is being modeled. Similarly, the mass flux of pyrolyzed gas, $\dot{m}_g$ and composition of pyrolyzed gas, Y_g, is only used if a charring ablator is being modeled. This case is not considered in this article.

4.0 ILLUSTRATIVE EXAMPLES

In this section, the application of the coupled, computational framework presented above to two types of air-graphite systems is described. In the first example, ablation of a graphite sample in a subsonic, high-enthalpy nitrogen flow produced in an Inductively Coupled Plasma (ICP) torch facility is considered. In this detailed example, it is shown that increasing the fidelity of the physical models used to simulate the flow-material interaction by including the response of the material greatly improves the agreement of the numerical results with the experimental data. In the second example, the ablation of a graphite TPS on a ballistic vehicle re-entering the Earth's atmosphere is considered, and the numerical results are compared with previously published numerical results. This example highlights the significant effect that the uncertainty in the type of chemical reaction mechanisms occurring at the surface has on the predicted surface properties.

4.1 Graphite ablation by nitrogen

CFD models can be used for simulating environments that cannot be studied in an experimental test facility. These models can be used for accurately predicting the aerothermal environment of the vehicle TPS during entry, but these models can be used to perform such analysis only after they have been validated for physical accuracy by comparison with experimental measurements.

This section presents an example of the study of gas-surface interactions that occur on a vehicle surface during its entry into a planetary atmosphere using the FRSC model along with an analysis of ablation using MOPAR2. The section first provides a brief description of the experimental facility at the University of Vermont used for assessment of the computations, followed by a description of the numerical setup used in this work along with the surface reactions investigated to study gas-surface interaction processes. The results of the numerical simulations and their comparison with the experimental measurements are presented thereafter.

4.1.1 Experimental Facility

Experimental tests were conducted by Professor Doug Fletcher and his graduate students in a 30 kW Inductively Coupled Plasma (ICP) Torch Facility at the University of Vermont [21, 22]. The ICP torch facility is designed to test scaled material samples in high enthalpy gas flows for simulation of planetary entry and Earth atmosphere re-entry trajectory heating conditions. It is configured for operation with subsonic flow to simulate post shock conditions of high enthalpy flight for a stagnation point geometry. The facility test conditions can be extrapolated to flight conditions by matching three parameters at the edge of the boundary layer, i.e., the

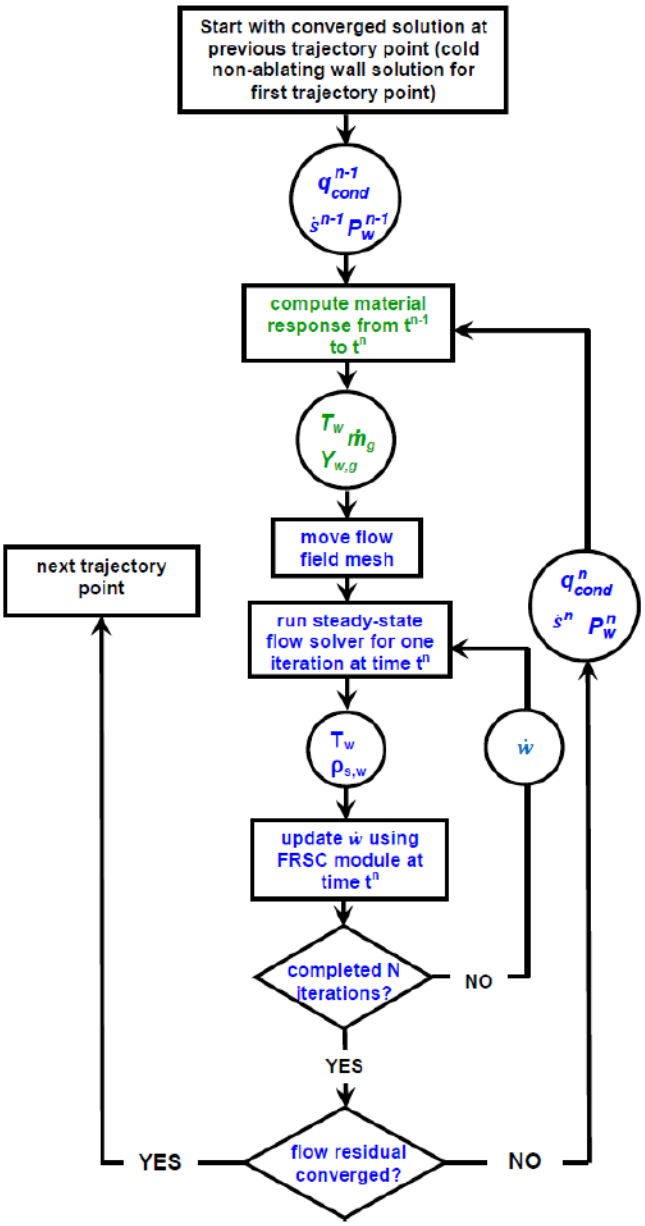

Figure 5: Coupling scheme between LeMANS-FRSC and MOPAR/MOPAR2.

enthalpy, the stagnation pressure and the velocity gradient. The stagnation point heat flux in the flight is equal to that in ground tests if these parameters are matched [23].

The facility is primarily comprised of the power supply unit, gas injection system and plasma test chamber. The gas injection system provides the nitrogen gas at room temperature that enters into the quartz confinement tube where hot nitrogen plasma is generated through an induced RF magnetic field created by a helical load coil. The hot nitrogen plasma then flows out of the quartz tube from the top into the test chamber of the ICP facility where the sample is tested. The test chamber is constructed from stainless steel and the torch locations with the highest heat loads are actively cooled with a closed loop water system. The test article is installed in a brass sample holder and the back space side of the sample is water cooled.

For this investigation, experimental results from graphite samples tested in the nitrogen plasma stream are used. The test articles are constructed from DFP2 grade graphite, fabricated by POCO Graphite [24]. Most ablative heat shields are designed from carbon-based matrix materials impregnated with low temperature phase change polymer resins that pyrolyze leaving a carbon rich char layer. Since the carbon layer continues to interact with the boundary layer gases, reactions between this layer and the gas-phase particles are of immense interest and therefore graphite is used for this study. Graphite is non-charring and therefore pyrolysis gases are not produced. Figure 6 shows a photograph of the graphite article during exposure to the nitrogen plasma in the test chamber of the ICP Torch Facility.

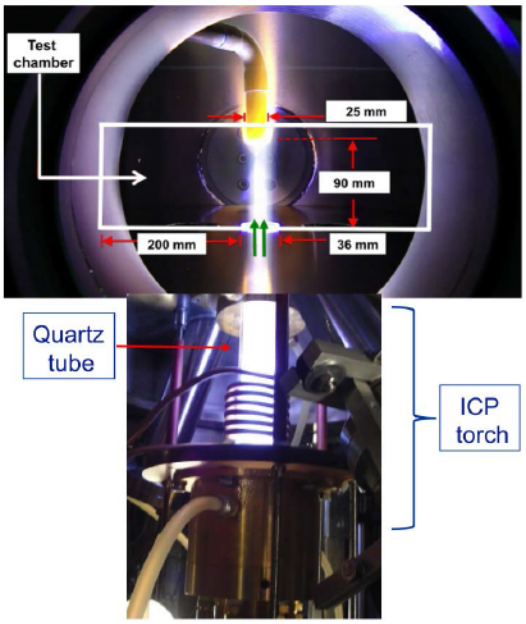

Figure 6: Experimental set up with graphite test article in nitrogen plasma in the test chamber of the ICP torch facility (section in box is the portion simulated using the CFD code LeMANS) (Source: Prof. D. G. Fletcher [21]).

The quantities measured are the surface heat flux, surface temperature, relative nitrogen atom number density and translational temperature in the reacting boundary layer above the graphite surface [22]. The stagnation region heat transfer is measured with a copper slug calorimeter. The surface temperature is measured using a two-color infrared optical pyrometer with a temperature range from 1273 to 3273 degrees K. The experimental tests measure the nitrogen atom number density and translational temperature in the reacting boundary layer above the graphite surface using a two-photon laser induced fluorescence (LIF) technique. Unfortunately, the

calibrated absolute atom number density values are not available. Therefore, the relative nitrogen atom number density is used for assessing the computational simulations. The graphite sample mass loss (ablation) rate is also quantified from pre- and post-test mass measurements.

4.1.2 Numerical Setup

The flow field conditions at the facility inlet (and therefore at the ICP Torch exit) are used to set the inlet boundary condition for the CFD simulation, in order to compare the computational results with the experimental measurements. The simulations are performed for the experimental conditions that are shown in Table 1. The test article is a 25 mm diameter graphite sample mounted at a distance of 90 mm from the quartz tube exit. The experimental set up with the graphite test article in the nitrogen plasma in the test chamber of the ICP torch facility is shown in Fig. 6.

Table 1: Freestream and wall boundary conditions.

Mass flow rate, (kg/s)	Temperature, [K]	Pressure, [kPa]	Wall Temperature, [K]
$0.82\text{x}10^{-3}$	7000	21.3	1598

The equilibrium composition of the nitrogen gas mixture at the quartz tube exit for the given temperature and pressure [21] are calculated using the NASA program Chemical Equilibrium with Applications (CEA) [25]. The species present in the gas mixture are molecular and atomic nitrogen with mole fractions of 0.15 and 0.85, respectively. The results of the computations show a significant level of nitrogen dissociation when chemical equilibrium is assumed at the quartz tube exit. The boundary conditions assigned for the simulations are shown in Fig. 7. An axisymmetric configuration is used for all simulations. In addition, the stagnation point is also shown where the heat flux and the surface temperature are measured.

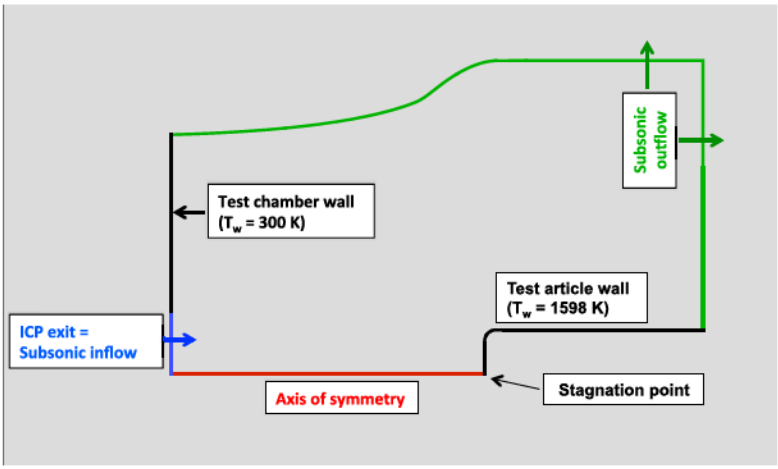

Figure 7: Boundary conditions.

4.1.3 Surface Reactions

The gas-surface interaction processes studied are the recombination of nitrogen atoms to molecules at the surface due to catalysis, and carbon nitridation where nitrogen atoms react with the surface carbon to form gaseous CN. Carbon nitridation is studied because sample mass loss is observed in the experiment and results for the surface recession are reported in the work by Lutz *et al* [21, 26]. Therefore, two sets of surface reactions are taken into account using the FRSC model. The first set is shown in Equation 25, and accounts only for recombination of nitrogen atoms on the surface of the graphite sample due to surface catalysis. In Equation 25, a gaseous nitrogen atom is adsorbed onto an available active site on the surface through an adsorption reaction. Then, another nitrogen atom from the gas phase recombines with the adsorbed nitrogen atom to form a gaseous nitrogen molecule and leaves the active site. The parameters k_{f1} and k_{f2} in these reactions are the respective forward reaction rates.

$$\begin{aligned} &N + (s) \xrightarrow{k_{f1}} N(s)\text{: Adsorption } (E_{ad} = 0 \text{ J/mol}) \\ &N + N(s) \xrightarrow{k_{f2}} N_2 + (s)\text{: Eley-Rideal recombination } (E_{ER} = 0 \text{ J/mol}) \end{aligned} \tag{25}$$

The second set of surface reactions, shown in Equation 26, takes into account recombination of nitrogen atoms due to surface catalysis as well as carbon nitridation. In the carbon nitridation process, carbon from the surface reacts with the impinging nitrogen atoms. The Eley-Rideal recombination reaction is used to represent the process of carbon nitridation. The parameters k_{f1}, k_{f2} and k_{f3} in these reactions are the respective forward reaction rates.

$$\begin{aligned} &N + (s) \xrightarrow{k_{f1}} N(s)\text{: Adsorption } (E_{ad} = 0 \text{ J/mol}) \\ &N + N(s) \xrightarrow{k_{f2}} N_2 + (s)\text{: Eley-Rideal recombination } (E_{ad} = 0 \text{ J/mol}) \\ &N + (s) + C_b \xrightarrow{k_{f3}} CN + (s)\text{: Eley-Rideal recombination } (E_{ad} = 0 \text{ J/mol}) \end{aligned} \tag{26}$$

All the test cases are investigated using a constant reaction efficiency γ. The effective reaction efficiency for a gas phase reactant consumed in a surface reaction process is the net result of competing finite-rate processes. An analytic expression for constant reaction efficiency γ is derived [27] for both of the surface reaction sets shown in Equations 25 and 26.
The net constant reaction efficiency γ for the surface reaction set shown in Equation 25 is given by,

$$\gamma = \frac{2S_0\gamma_N}{S_0 + \gamma_N} \tag{27}$$

The net constant reaction efficiency γ for the surface reaction set shown in Equation 26 is given by,

$$\gamma = \frac{2S_0\gamma_N + \gamma_{CN}\gamma_N}{S_0 + \gamma_N} \tag{28}$$

In Equations 27 and 28, γ_N is the reaction efficiency for surface catalysis, and γ_{CN} is the carbon nitridation efficiency. A constant catalytic efficiency is achieved by setting S_0 equal to γ_N. It is assumed in this investigation that all the carbon mass loss occurs due to the carbon nitridation reaction.

4.1.4 Baseline Results

The test cases considered in this study to determine the effects of gas-surface interaction processes are shown in Table 2.

Table 2: Test cases.

Case	Catalytic efficiency γ_N	Carbon nitridation efficiency γ_{CN}	Effective reaction efficiency γ
Case 1	0	0	0
Case 2	0.07	0	0.07
Case 3	0.07	0.005	0.0725
Case 4	1	0	1

The catalytic efficiency γ_N is set to zero for a non-catalytic wall and is set to 1 for a fully catalytic wall. The partially catalytic wall condition of γ_N = 0.07 is based on an experimentally determined value [28] for pure carbon. The catalytic efficiency was obtained from the comparison of measured data of heat transfer to the carbon specimen in subsonic jets of dissociated nitrogen with the numerical computations of heat transfer. The value γ_{CN} = 0.005 for Case 3 is set based on a value determined by Driver and Maclean [29]. It is obtained from a comparison between data from arc jet tests performed for Phenolic Impregnated Carbon Ablator (PICA) in nitrogen and results from computational simulations. The nitridation efficiency of γ_{CN} produces good predictions of both heat transfer and recession rate when both reactions, i.e., carbon nitridation and nitrogen atom recombination to nitrogen molecules due to catalysis, are included in the computations [29]. It should be noted that γ_{CN} is dependent on the type of carbon used as well as the experimental conditions. Case 1 represents a wall where no surface chemistry is accounted for and is treated as non-catalytic.

The test article wall is set to a radiative equilibrium boundary condition and the test chamber wall is set as an isothermal wall with a temperature of 300 K. A uniform velocity, temperature and density profile at the facility inlet is specified in the simulations. Since the flow at the inlet of the test chamber is non-uniform, a study is performed to assess the effects of different inlet profiles on the species concentration and temperature gradients near the material surface, and on the heat transfer to the material surface. It is concluded that the non-uniform inlet profile does not significantly affect the solution. The results for the study are discussed in Reference [30].

The translational temperature contours in the test chamber of the ICP facility obtained for Case 4 are shown in Figure 8. These contours show the evolution of hot nitrogen plasma in the test chamber on exiting the the ICP torch. The velocity streamlines show that the flow enters from the ICP torch exit on the left and impinges on the graphite sample at the right.

The results along the stagnation line in the boundary layer are shown for the translational temperature in Figure 9 and the normalized nitrogen atom density in Figure 10. There is an increase in temperature in the boundary layer for cases where surface chemistry is included as compared to Case 1 a for non-catalytic wall. The comparisons between Cases 2, 3 and 4 show that temperature in the boundary layer is not significantly affected for different surface chemistry models. There is an increase in nitrogen atom density in the boundary layer for Case 1, whereas it is consumed for all other cases due to surface chemical reactions. The nitrogen atom loss is due the catalytic recombination of nitrogen atoms to molecules for Cases 2 and 4. The nitrogen

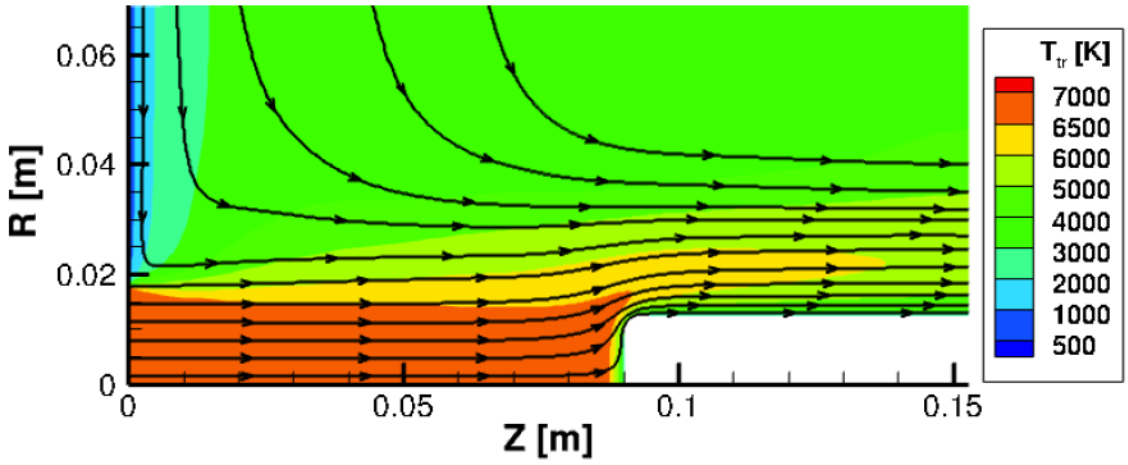

Figure 8: Translational temperature contours for the flowfield in the test chamber of the ICP facility obtained for Case 4 (γ_N=1).

atom loss seen for Case 3 is the combined effect of surface catalysis as well as carbon nitridation. The nitrogen atom density for all cases except Case 1 show good agreement with the experimental measurements.

The effect of surface chemistry on the surface properties is also evaluated. The total heat flux is plotted in Figure 11(a) and the diffusive heat flux is plotted in Figure 11(b). An increase in the total heat flux is seen in all the cases with surface reactions as compared to the non-catalytic wall case. This increase is explained by the contribution from diffusive heat flux for the cases with surface reactions, which is zero for a non-catalytic wall. Figure 12 shows the surface temperature predicted using each chemistry model. Case 4 (fully catalytic surface) results in the highest predicted surface temperature, while Case 1 (no surface chemistry) results in the lowest predicted surface temperature. The temperature for Cases 2 and 3 lie between those for non-catalytic and fully catalytic walls.

The carbon mass removal flux as a result of the carbon nitridation reaction for Case 3 is also computed and is shown in Figure 13. The total mass loss rate is calculated from $\dot{m}_b$ as shown in Equation 29.

$$\text{mass loss rate} = \int \dot{m}_b dA \tag{29}$$

where $\dot{m}_b$ is the mass removal flux calculated using Equation 15 for each surface element and dA is the surface area of each element. The stagnation point heat flux is measured experimentally using a slug calorimeter for test conditions similar to this case. The heat flux is measured for the case of 0.84 g/s mass flow rate and pressure of 21.3 kPa.

A comparison between the experimental and computed values for stagnation point heat flux, temperature and mass loss rate for Case 3 is provided in Table 3. The computational values are much higher than the experimentally measured values; this difference may be explained by the combined effect of various mechanisms. It could be attributed to a higher degree of nitrogen atom flux to the surface in the calculations. An assumption of chemical equilibrium of the nitrogen gas mixture at the ICP torch exit is used in these simulations, however, this assumption likely overpredicts the degree of dissociation for this type of chemically reacting flow with finite-rate chemistry flow. Therefore, actual flux of dissociated nitrogen atoms to the test sample might be less than what is predicted in these simulations, and a reduction in nitrogen atom flux to the surface would result in

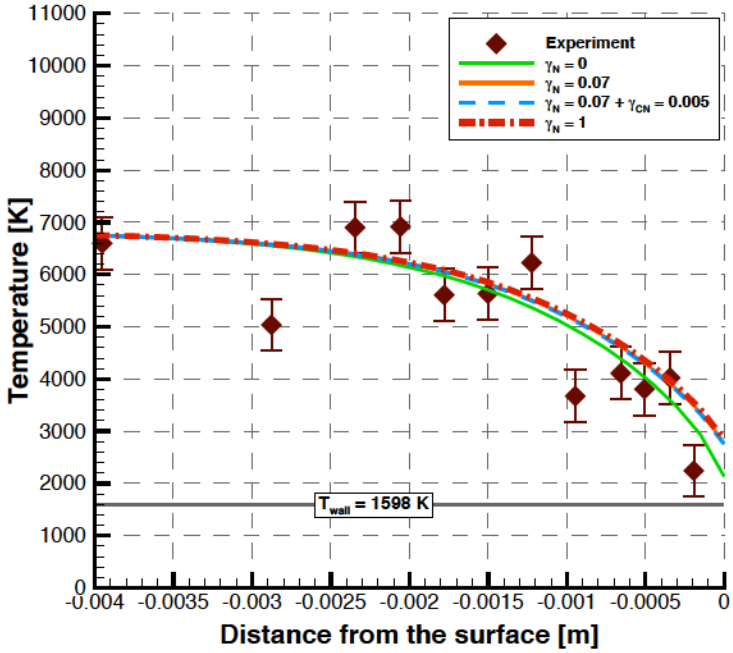

Figure 9: Comparison of translational temperature along the stagnation line.

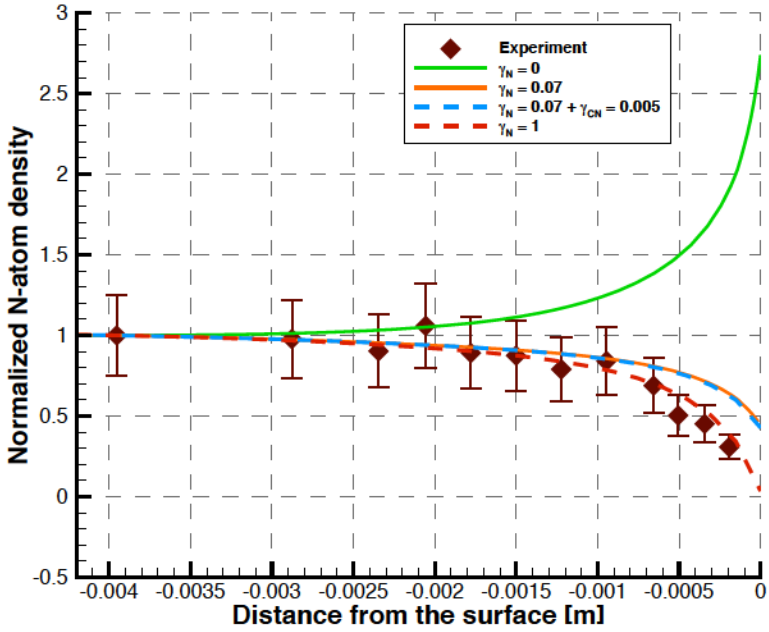

Figure 10: Comparison of normalized N-atom density along the stagnation line.

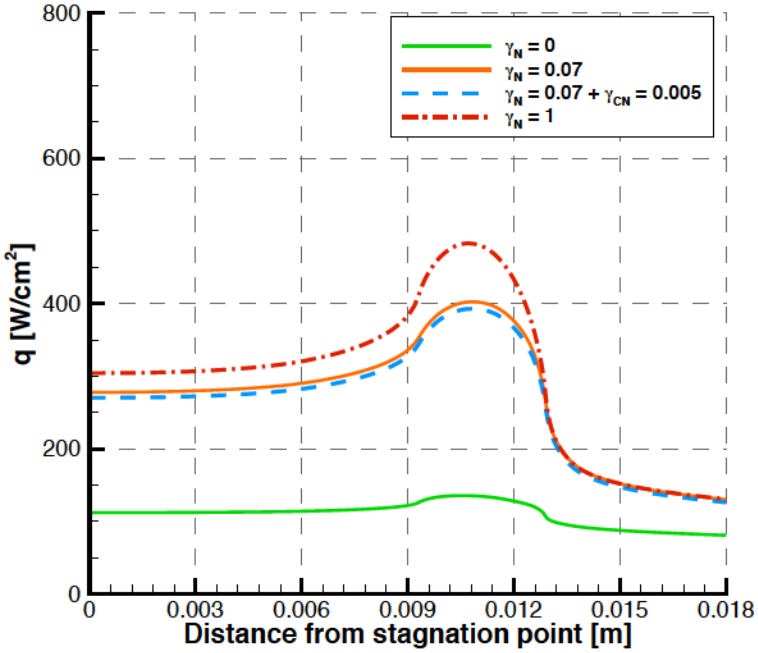

(a) Total heat flux

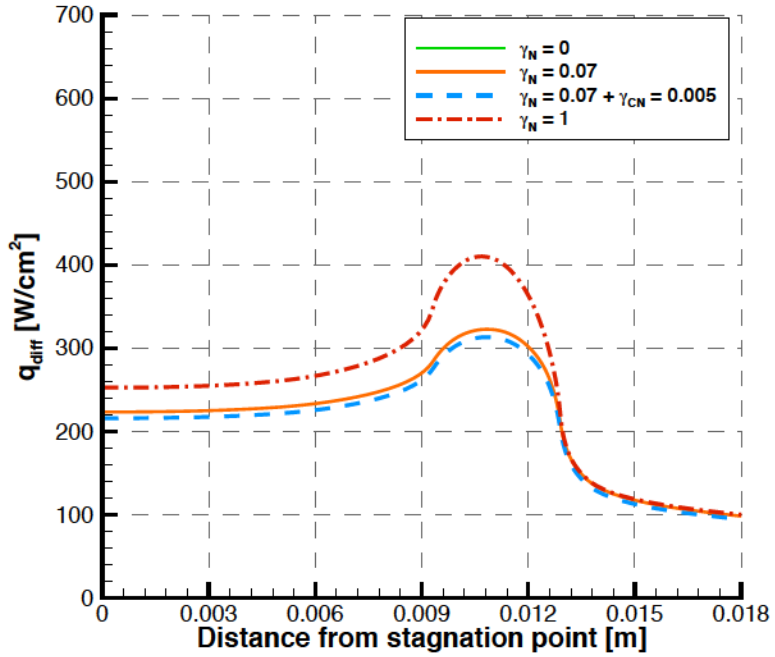

(b) Diffusive heat flux

Figure 11: Comparison of wall heat flux between the computational results.

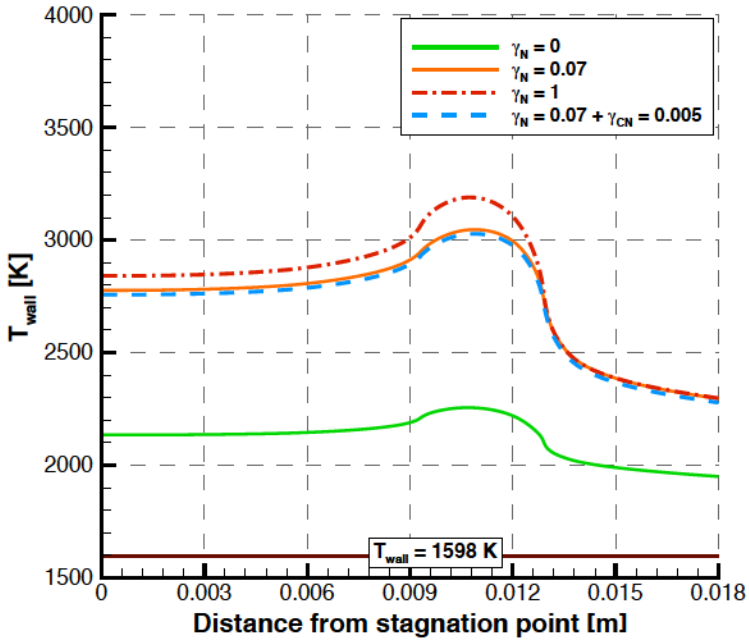

Figure 12: Comparison of wall temperature between the computational results.

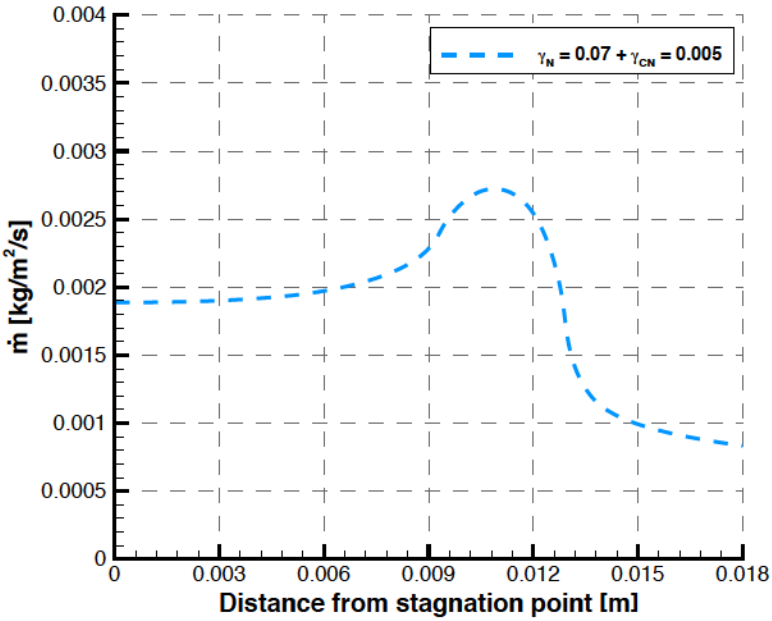

Figure 13: Mass removal flux due to carbon nitridation.

a reduction in the mass removal rate. The computed values of heat flux, wall temperature and mass loss rate could also be affected by the net heat transfer to the surface. A radiative equilibrium boundary condition is used in these simulations and the heat conduction within the sample is not included, which if accounted for, may affect the surface properties.

Table 3: The stagnation point values and the mass loss rate.

	$q_{stag}[W/cm^2]$	$T_{stag}[K]$	Mass loss rate $[mg/s]$
CEA	270	2757	2.2
Experiment	40 - 80	~1600	0.2 - 0.6

4.1.5 Effect of Inlet Composition

Based on these baseline results, the estimated power that is absorbed by the flow in the ICP torch is used to determine the composition of the gas at the test chamber inlet. The power in the flow is the product of the voltage, current, and an efficiency factor estimated to be 0.56 [31], resulting in an estimated 13.8 kW of power deposited in the flow. The flow power is related to the mass flow rate through the torch, and the temperature and composition of the gas as shown in Equation 30.

$$Power = \dot{m}_{flow}\Delta h \tag{30}$$

$$\Delta h = \sum_{i=N,N_2} Y_i \int_{298}^{T} C_{pi}\, dT + \sum_{i=N,N_2} Y_i \Delta \overset{\circ}{h}_{fi}$$

where,

$$Y_i = \frac{M_i}{M_{avg}} X_i \; ; \; M_{avg} = \sum_{i=N,N_2} X_i M_i$$

where X_i is the species mole fraction, M_i and M_{avg} are the individual species and average gas mixture molecular weight, respectively. C_{pi} is species specific heat at constant pressure (including internal energy modes) and $\overset{\circ}{h}_{fi}$ is the species heat of formation.

The composition of the gas mixture is calculated for 13.8 kW power using the mass flow rate and inlet temperature given in Table 1. This section presents the comparison performed between the results obtained using the inlet gas composition calculated assuming chemical equilibrium and those obtained for a flow power of 13.8 kW. The power in the flow corresponding to a chemical equilibrium composition at the inlet, and an inlet temperature of 7000 K, corresponds to 30 kW, which is 100% higher than the calculated power. The comparison is performed for Case 3 to include the effects of the inlet gas composition on carbon mass removal.

The relation of power with gas mixture composition is shown in Figure 14 where power is plotted against nitrogen atom mole fraction X_N for constant temperature of 7000 K along with the constant power of 30 kW in the flow for chemical equilibrium composition at the inlet. The power in the flow is minimum for zero nitrogen atom mole fraction such that the flow is not dissociated. The flow power increases with the level of dissociation in the flow and reaches a maximum value for fully dissociated flow (X_N = 1).

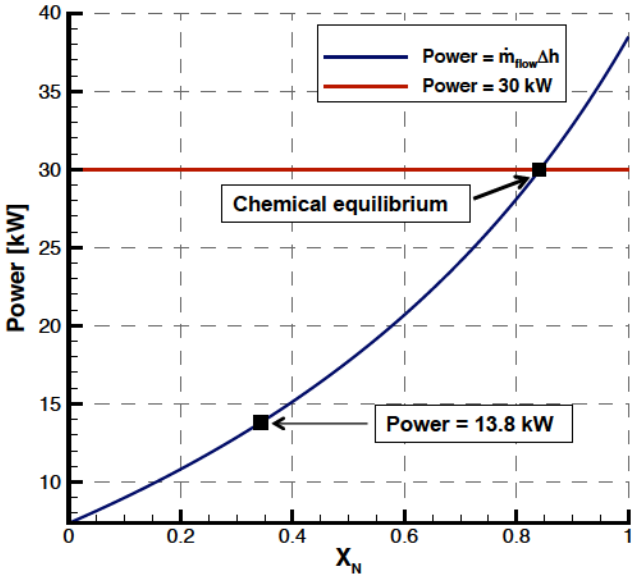

Figure 14: Deposited power as a function of nitrogen atom mole fraction.

Based on the chemical equilibrium and 13.8 kW inlet compositions, the translational temperature and normalized nitrogen atom number density profiles along the stagnation line in the boundary layer are shown in Figures 15 and 16, respectively. The translational temperature in the boundary layer for 13.8 kW power is lower in comparison to the equilibrium inlet composition because the temperature in the flow decreases with decrease in enthalpy, and enthalpy is directly related to power. The results produced using the inlet composition calculated for 13.8 kW of deposited power show better agreement with the experimental data for normalized nitrogen atom number density when compared to the results produced by assuming an equilibrium composition at the inlet. The level of dissociation in the flow is higher for the chemical equilibrium inlet composition as compared to the 13.8 kW power inlet composition, leading to a larger nitrogen atom density in this case.

The total heat flux and temperature at the wall for these cases are shown in Figures 17 and 18, respectively. The mass removal flux is shown in Figure 19. There is a significant reduction in predicted heat flux, wall temperature and mass loss rate when the inlet composition corresponding to a deposited power of 13.8 kW is used. The comparison between the stagnation point values for the two cases along with the experimental data is shown in Table 4. There is a 52% reduction in heat flux, 17% reduction in wall temperature, and 60% reduction in mass loss rate for the assumption of 13.8 kW flow power when compared to the results generated with the use of an equilibrium chemical composition at the inlet. These values are still higher than the experimentally measured data. The losses in the ICP torch are not quantified experimentally and hence are not included in the calculation of power. The comparisons suggest that the power in the flow maybe even less than 13.8 kW.

4.1.6 Effect of Inlet Temperature

Since the ICP torch exit conditions are not well defined, a sensitivity analysis on the ICP torch exit chemical composition is performed for different values of inlet temperature and inlet power. To determine the sensitivity of the predicted flow and surface properties to inlet temperature, three values of inlet temperature, 6000 K, 7000 K, and 8000 K, are considered. The chemical composition at the inlet is calculated for 13.8 kW power, using the measured mass flow rate, and Equation 30. All the simulations are performed for Case 3 surface

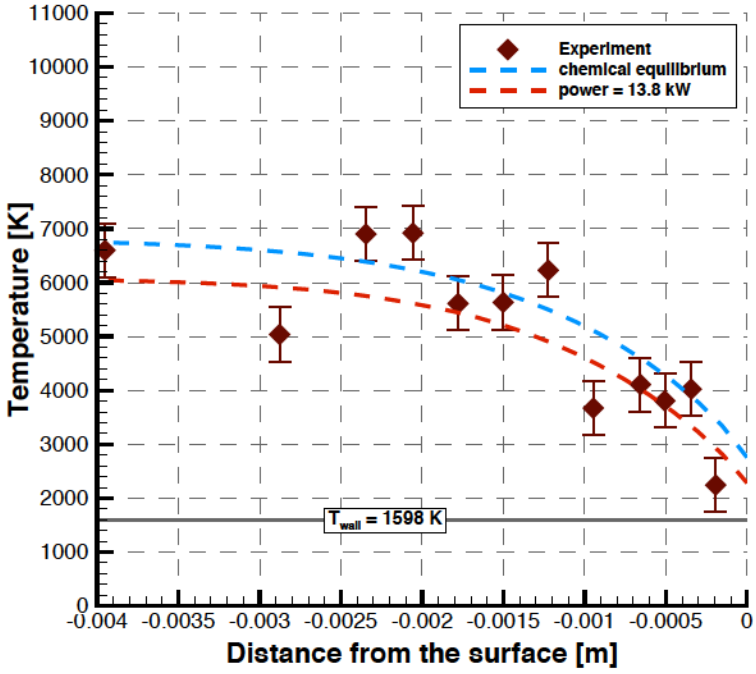

Figure 15: Comparison of translational temperature along the stagnation line for different inlet compositions.

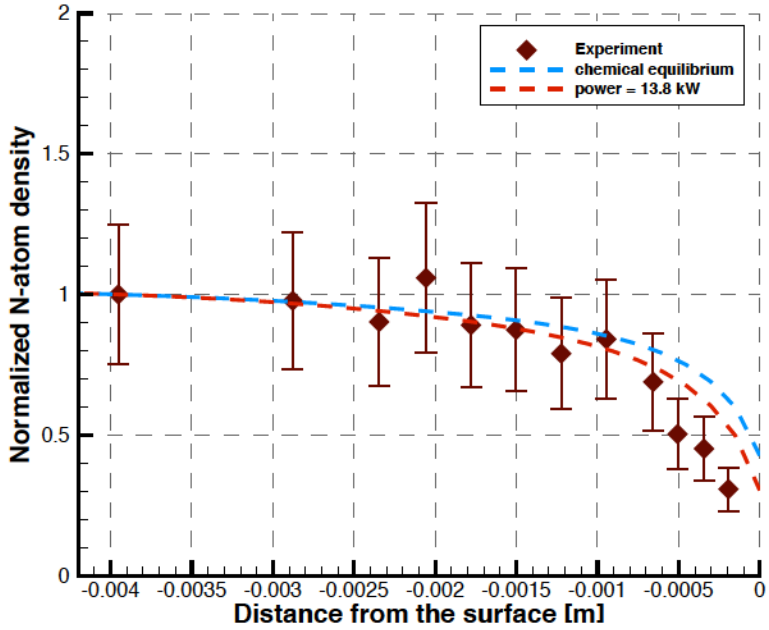

Figure 16: Comparison of normalized N-atom density along the stagnation line for different inlet compositions.

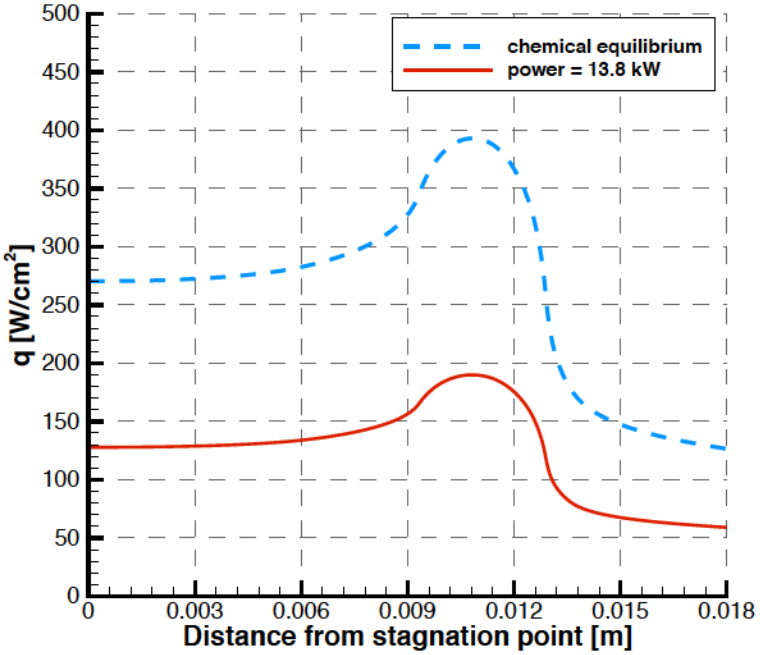

Figure 17: Comparison of wall heat flux between the computational results for different inlet compositions.

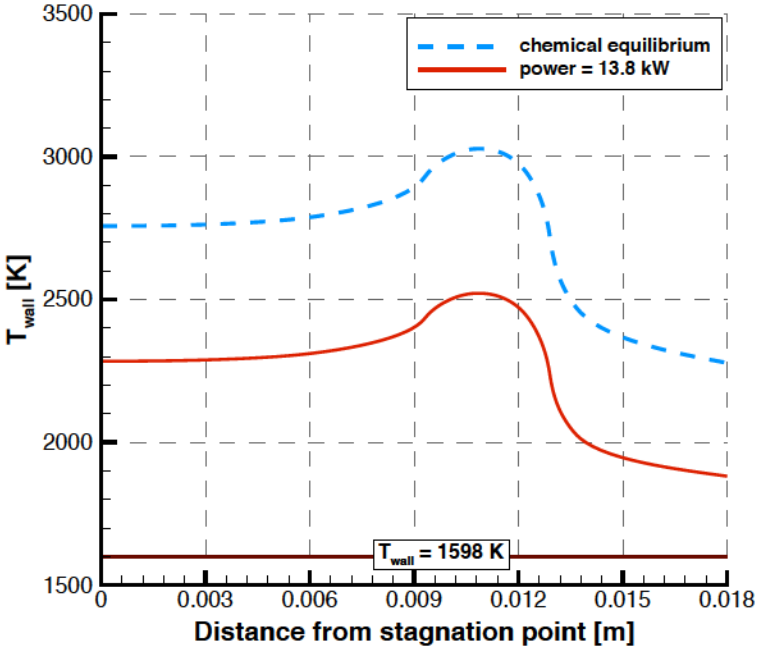

Figure 18: Comparison of wall temperature between the computational results for different inlet compositions.

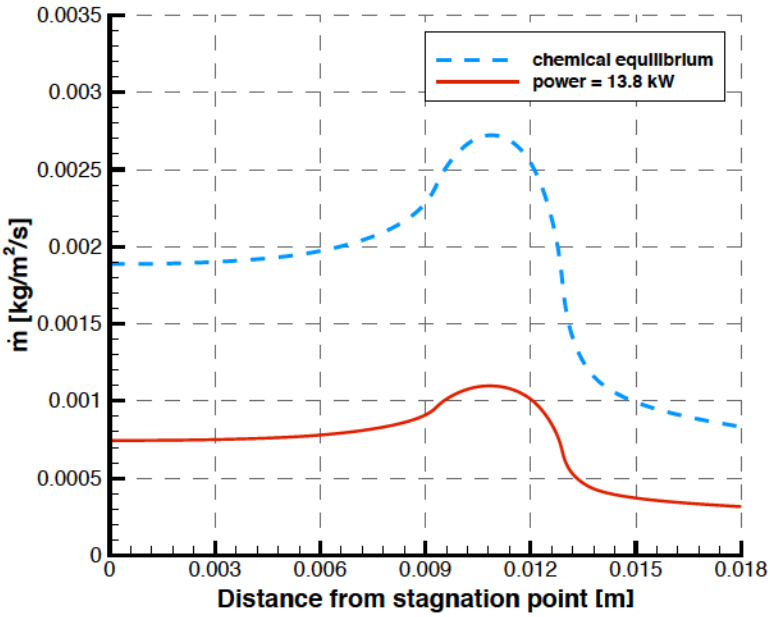

Figure 19: Comparison of mass removal flux between chemical composition for equilibrium inlet and 13.8 kW power.

Table 4: The stagnation point values and the mass loss rate.

inlet	T_{inf} [K]	$q_{stag}[W/cm^2]$	$T_{stag}[K]$	Mass loss $[mg/s]$
CEA	7000	270	2757	2.2
13.8 kW	7000	128	2284	0.86
Experiment	7000	40 - 80	1600	0.2 - 0.6

chemistry.

The predicted translational temperature and normalized nitrogen atom number density profiles are shown in Figures 20 and 21. These Figures show that there is negligible effect of varying inlet temperature on the profiles of translational temperature and the nitrogen atom density. The difference between each respective profile both for translational temperature and the nitrogen atom density is less than 1%. All three cases tend to reach a similar mixture composition and temperature since the power, and therefore the enthalpy, of the flow is constant. Similarly, there is only a small effect of varying inlet temperature on the predicted surface properties. The comparison between the stagnation point values and the mass loss rate for these cases is shown in Table 5. The heat flux, wall temperature and the mass loss rates increase with an increase in inlet temperature. The heat flux is increased by approximately 5%, wall temperature by 1%, and the mass loss by 4% for every 1000 K increase in temperature at constant power. The conclusion of this sensitivity study is that the effect of varying the inlet temperature, while holding the value of deposited power constant, on translational temperature and the nitrogen atom density in the boundary layer, surface heat flux, wall temperature and mass loss rate is relatively small and certainly much smaller than the uncertainties in the measurements.

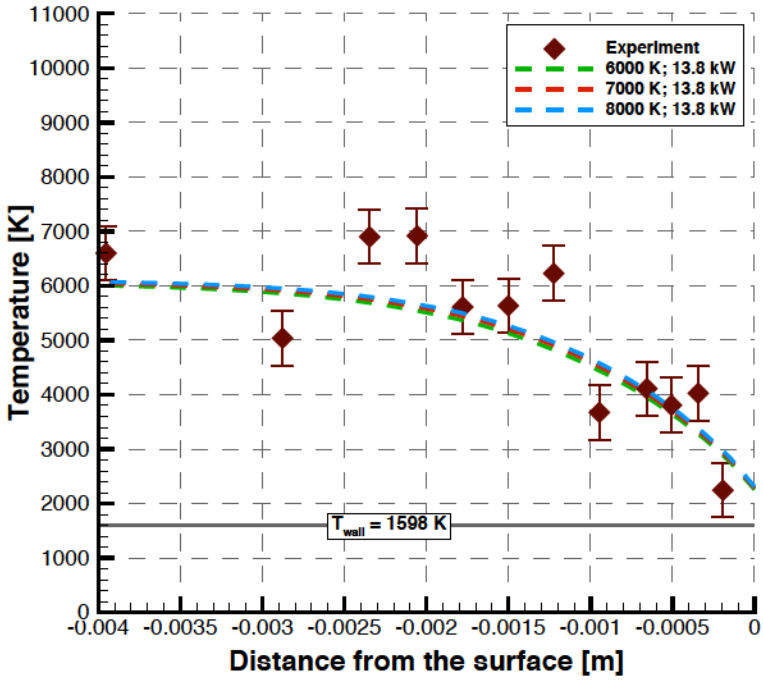

Figure 20: Comparison of translational temperature along the stagnation line in the boundary layer for various inlet temperatures.

4.1.7 Effect of Deposited Power

To determine the sensitivity of the predicted flow and surface properties to the amount of power deposited in the flow, and therefore to the inlet composition, the inlet temperature is held constant at the measured value of 7000 K, and the amount of power deposited in the flow is varied. The inlet composition is calculated using Equation 30, so that the power is varied by varying the concentration of nitrogen atoms in the plasma mixture exiting the ICP.

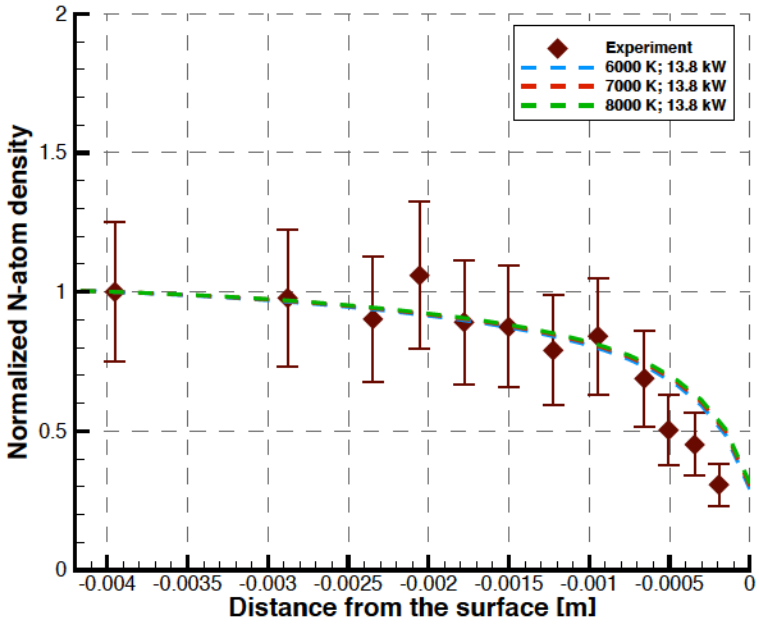

Figure 21: Comparison of normalized N-atom density along the stagnation line in the boundary layer for various inlet temperatures.

Table 5: Stagnation point values and mass loss rate for various inlet temperatures.

$Power[kW]$	T_{inf} [K]	$q_{stag}[W/cm^2]$	$T_{stag}[K]$	Mass loss $[mg/s]$
13.8	6000	122	2259	0.83
13.8	7000	128	2284	0.86
13.8	8000	133	2308	0.89
Experiment	7000	40 - 80	1600	0.2 - 0.6

The translational temperature profile along the stagnation line in the boundary layer is shown in Figure 22. The respective profiles for 13.8 kW and 30 kW (chemical equilibrium) power are also included in the Figure. The difference between the translational temperature profile in the boundary layer is within 1% for a change in power from 7.3 kW to 9.0 kW, 2% for 9.0 kW to 10.8 kW, 5% for 10.8 kW to 13.8 kW, and within 13% for 13.8 kW to 30 kW. These results shows that the predicted temperature is sensitive to the change in power. This is because the temperature in the flow increases with increasing enthalpy, and enthalpy is directly related to deposited power.

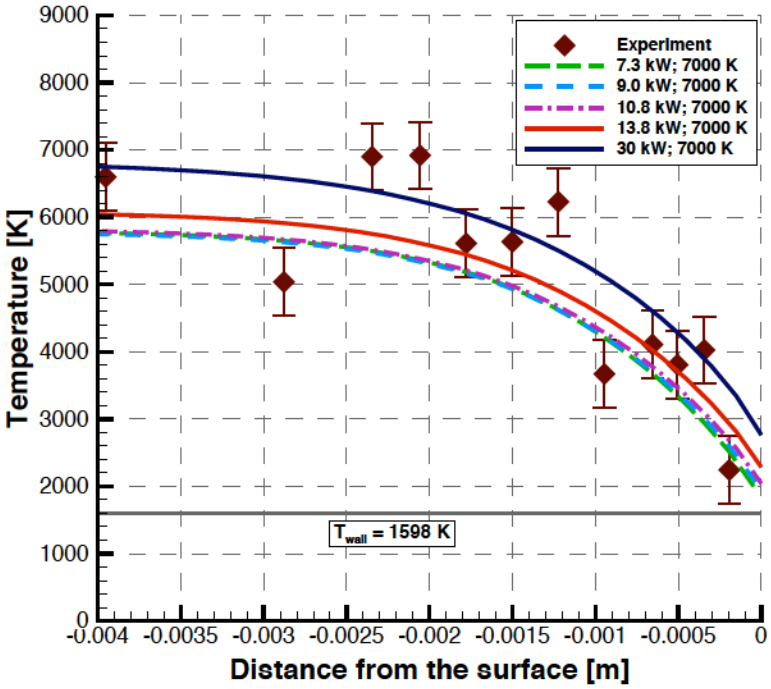

Figure 22: Comparison of translational temperature along the stagnation line in the boundary layer for various values of deposited power.

The normalized nitrogen atom number density along the stagnation line in the boundary layer is shown in Figure 23. The profiles for 13.8 kW and 30 kW (chemical equilibrium) power are also included in the Figure. The normalized nitrogen atom density is not significantly affected by power. This is because these profiles are self normalized and the trend in the profiles is the same. Also, for all the conditions, the surface chemistry considered is the same. The case with 30 kW power shows a difference of 10% from the 13.8 kW profile for the region close to the sample. The reason for this is that the 30 kW case is highly dissociated with a mole fraction of 0.85 at the inlet, and the same chemistry model is considered in all cases. This leads to a higher density of nitrogen atoms in the vicinity of the test sample as compared to the cases with less deposited power and therefore lower levels of flow dissociation.

Even though the normalized nitrogen atom density is not significantly affected by varying power, the absolute nitrogen atom number density is considerably affected as shown in Figure 24. There is an approximately 117% increase in the atom number density in the boundary layer when the power is increased from 7.3 kW to 9.0 kW, a 48% increase for the variation in power from 9.0 kW to 10.8 kW, a 68% increase for 10.8 kW to 13.8 kW, and a 65% for 13.8 kW to 30 kW. The absolute nitrogen atom number density increases with increasing power deposition and enthalpy because a greater percentage of the flow is dissociated at these con-

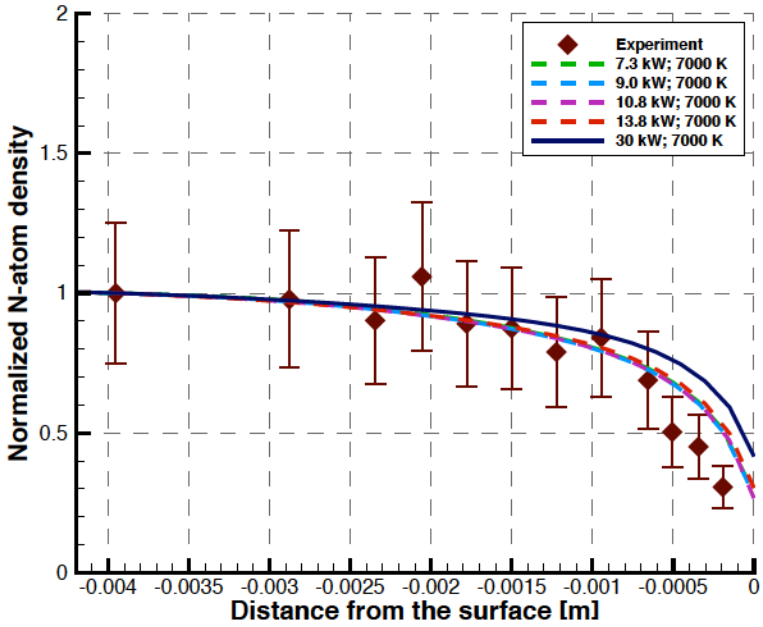

Figure 23: Comparison of normalized N-atom density along the stagnation line in the boundary layer for various values of deposited power.

ditions. These results show that the relative values for different test conditions can have similar profiles but the respective absolute values can vary considerably. It can be concluded from these results that it is important to obtain absolute measured values for nitrogen atom number densities for validation of computational results with experimental data.

The total heat flux and temperature at the wall for these cases are shown in Figures 25 and 26. The mass removal flux is shown in Figure 27. The wall heat flux, wall temperature and the mass loss increase with increasing levels of deposited power. This increase is explained by the associated increase in flux of nitrogen atoms at the test article surface, which recombine at the surface catalytically and release the heat of recombination to the surface. This process results in an increase in the heat flux and wall temperature along the surface of the test article. The increased flux of nitrogen atoms also causes more carbon nitridation and an increase in mass loss.

The comparison between the stagnation point values and the mass loss rate for these cases along with the experimentally measured values is shown in Table 6. It can be concluded from these results that the translational temperature and the nitrogen atom density in the boundary layer, surface heat flux, wall temperature and mass removal flux along the test article surface are very sensitive to the amount of power deposited in the flow. Therefore, it is very important to experimentally characterize the power absorbed by the plasma in the ICP torch. The necessity of experimental measurements of absolute atom number densities is again shown by these results. The amount of nitrogen atom flux in the boundary layer directly affects the heat transferred to the surface, the surface temperature, and the mass loss rate. This means that the absolute number density is required to draw conclusions about the surface chemistry models as well as the surface reactions involved.

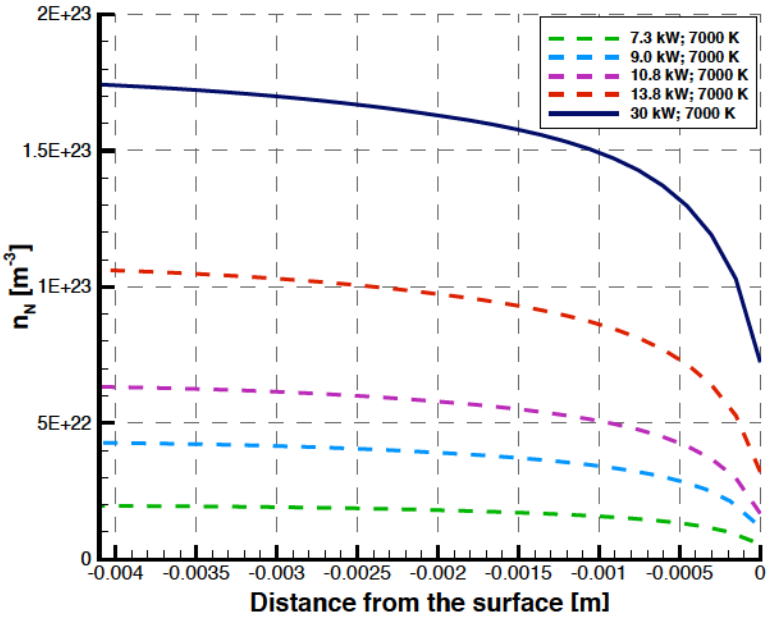

Figure 24: Comparison of N-atom number density along the stagnation line for various values of deposited power.

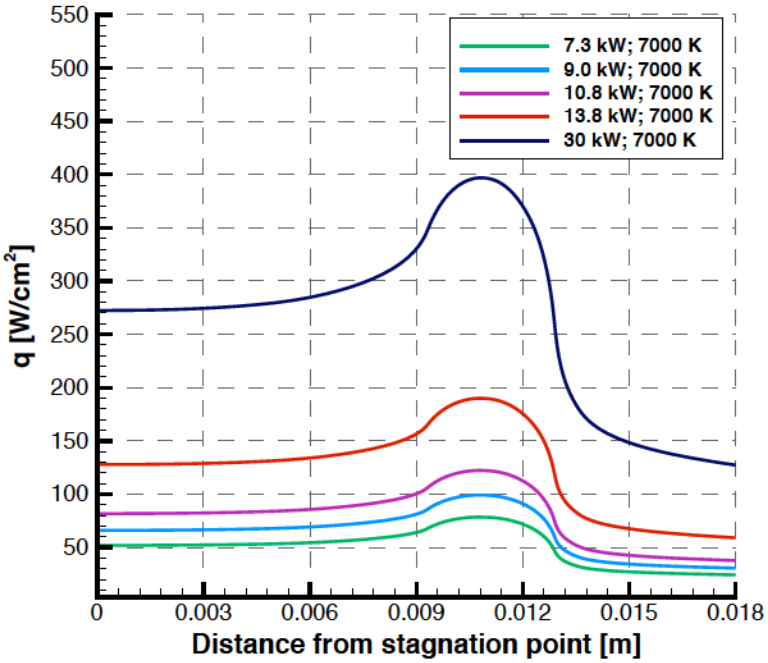

Figure 25: Comparison of wall heat flux between the computational results for various values of deposited power.

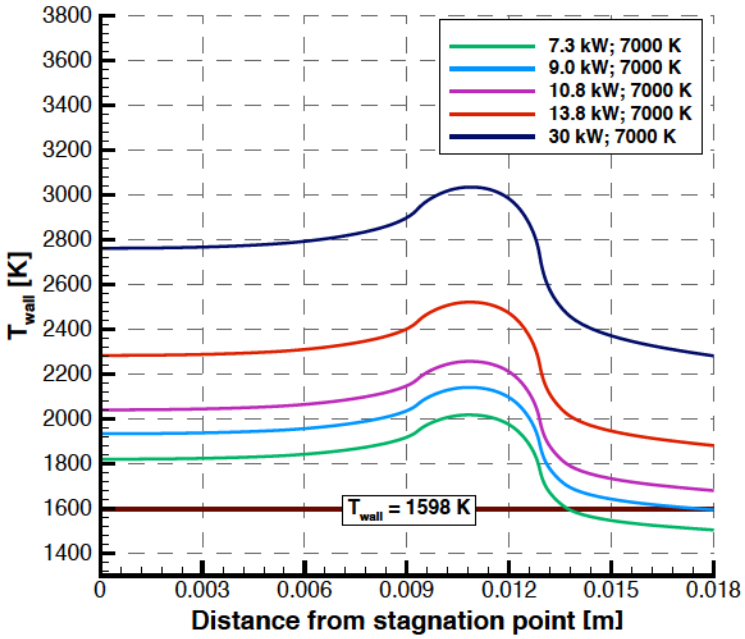

Figure 26: Comparison of wall temperature between the computational results for various values of deposited power.

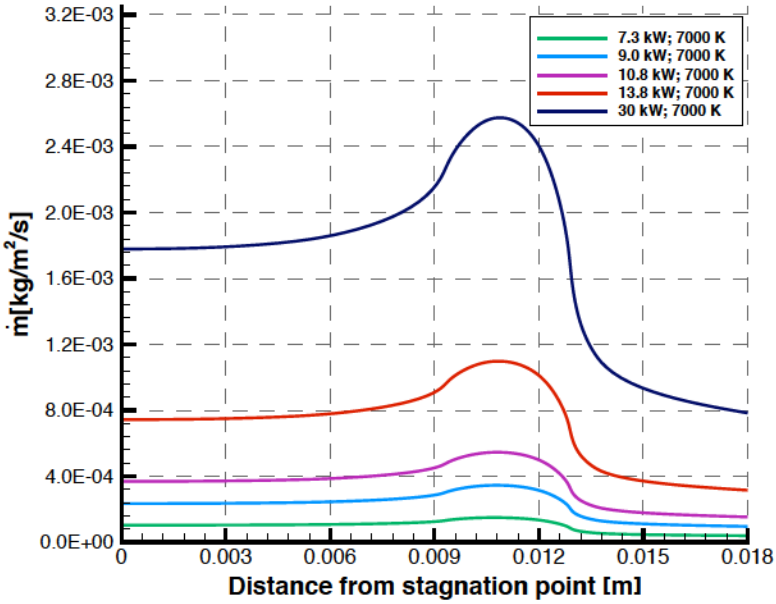

Figure 27: Comparison of mass removal flux for various values of deposited power.

Table 6: Stagnation point values and mass loss rate for various values of deposited power.

Power $[kW]$	X_N	T_{inf} [K]	q_{stag} $[W/cm^2]$	T_{stag} $[K]$	Mass loss $[mg/s]$
30	0.85	7000	270	2757	2.2
13.8	0.42	7000	128	2284	0.86
10.8	0.2	7000	82	2041	0.42
9.0	0.1	7000	66	1934	0.27
7.3	0	7000	52	1821	0.11
Experiment		7000	40 - 80	1600	0.2 - 0.6

4.1.8 Effect of Material Response

The last step in this study is to include the response of the graphite material in the analysis, since the net heat transfer to the wall is expected to have an impact on the surface properties. The contribution of conductive heat transfer within the sample is determined by using the material response code MOPAR2. The thermal conductivity, specific heat, and emissivity of DFP2 grade POCO Graphite [24] are used in MOPAR2. As shown in Table 6, the case with 9.0 kW of deposited power shows the best agreement with the experimental data for stagnation point heat flux and mass loss. Therefore, this case is used to investigate for the effects of conduction within the sample.

In this simulation, the heat flux at the surface of the sample that exposed to the flowfield is calculated using Equation 18. The temperature on the rear surface of the graphite sample is set to 350 K, based on the measured temperature of the rear surface of the copper slug [32]. This value is used because the temperature of the rear surface of the graphite test article was not measured experimentally. Additional simulations were run in which this value was varied with no significant effect on the predicted flow field and surface properties. In this simulation, MOPAR2 is run for 300 s, at which time the updated temperature at each cell face along the graphite surface is passed to LeMANS-FRSC. This time is chosen as the heat flux is measured experimentally after a 300 s exposure time to nitrogen plasma.

The results from this simulation are compared with the results for the radiative equilibrium wall boundary condition. The contours of temperature in the flowfield and within the solid test article are shown in Figure 28. In this picture, the legend $T_{flowfield}$ shows the variation of translational temperature in the flowfield and T_{solid} shows the variation of temperature within the solid. The flow enters from the ICP torch exit on the left and impinges on the graphite sample at the right. The front of the graphite sample is exposed to hot nitrogen plasma. The flow field contours of temperature show the way in which the hot nitrogen plasma evolves after exiting the ICP torch. The sample is at the highest temperature in the front region that is exposed to hot nitrogen plasma and it is the lowest at the rear surface that is maintained at a 350 K.

The stagnation line profiles for translational temperature and normalized nitrogen atom number density in the boundary layer are shown in Figures 29 and 30. There is no significant change in the temperature and normalized nitrogen atom number density in the boundary layer when conduction within the sample is included in the calculations. This is because the same flowfield conditions are employed in both simulations. However, in the vicinity of the surface, the temperature drops and the nitrogen atom density increases when conduction into the sample is considered. The reason for this is explained by the surface properties.

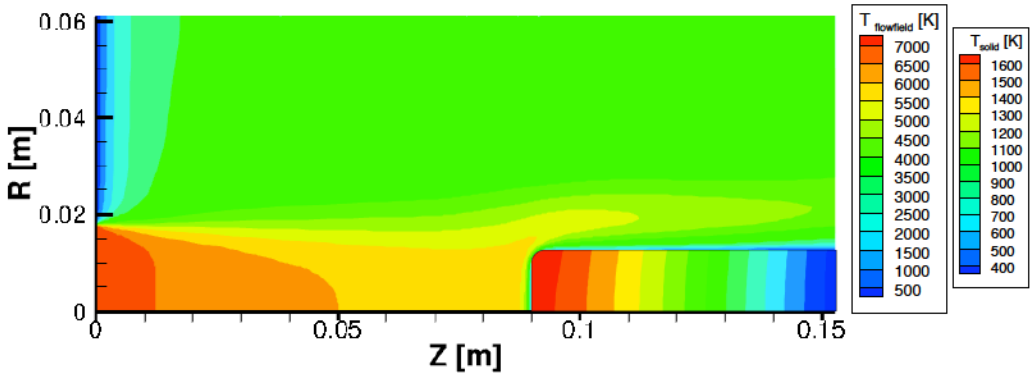

Figure 28: Temperature contours for the flowfield and within the solid test article.

Comparisons of the predicted total heat flux and the temperature of the surface of the sample are shown in Figures 31 and 32. There is an approximately 5% increase in heat flux and 17% decrease in temperature when heat is allowed to conduct into the material. The temperature decrease results in an increase in conductive heat flux because the temperature gradient at the wall increases. This decrease in temperature at the wall also reduces the temperature in the flow in the vicinity of the surface. When the temperature decreases, the density of nitrogen atoms increases to maintain constant pressure in the flow field.

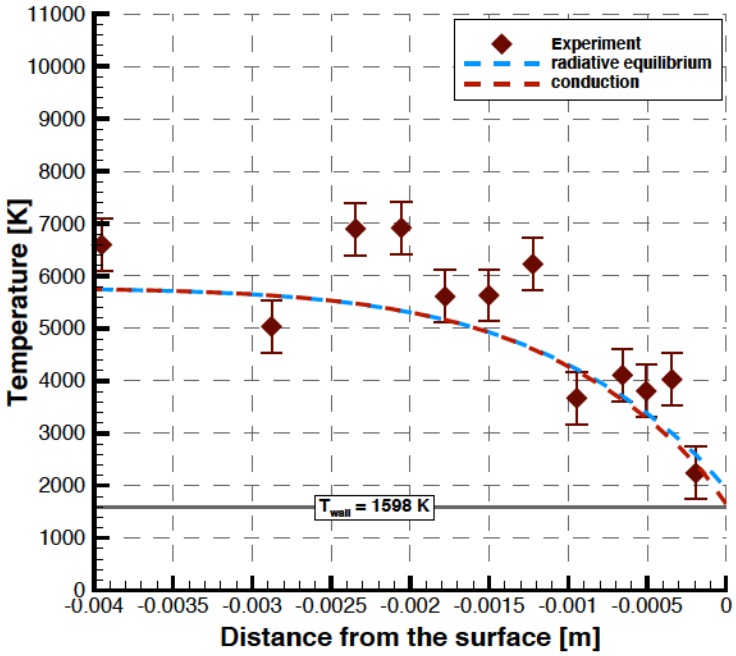

Figure 29: Comparison of translational temperature along the stagnation line in the boundary layer for different energy balance conditions at the wall.

The mass removal flux is shown in Figure 33. There is no significant effect of conduction within the sample on mass removal flux. This is because the mass removal flux depends on the nitrogen atom density and the

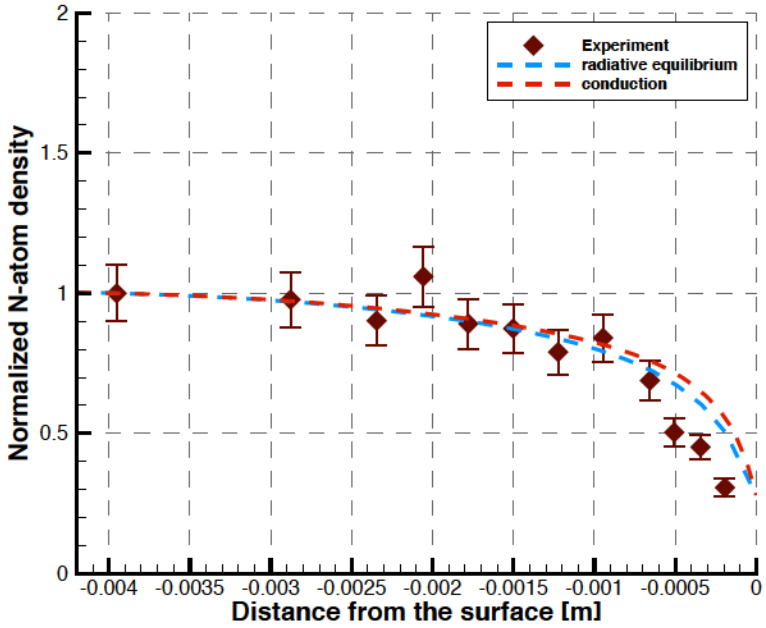

Figure 30: Comparison of normalized N-atom density along the stagnation line in the boundary layer for different energy balance conditions at the wall.

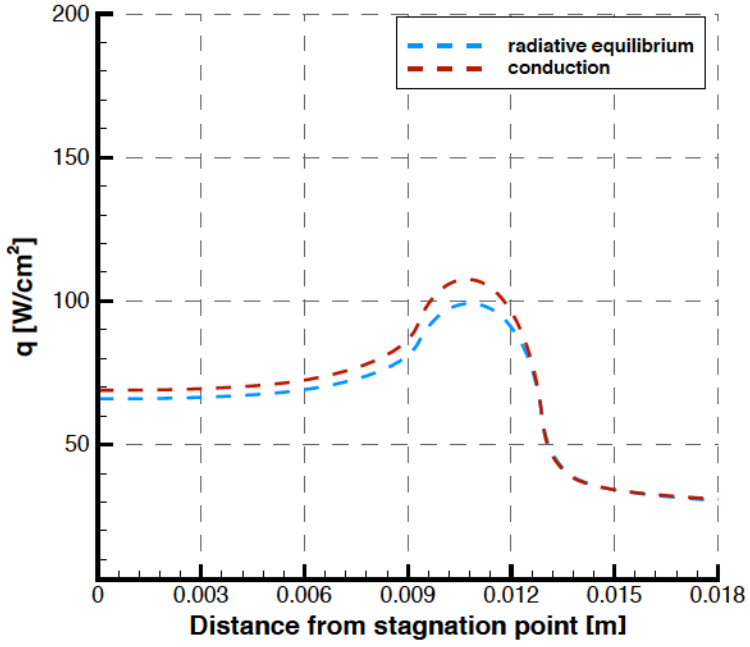

Figure 31: Comparison of wall heat flux for different energy balance conditions at the wall.

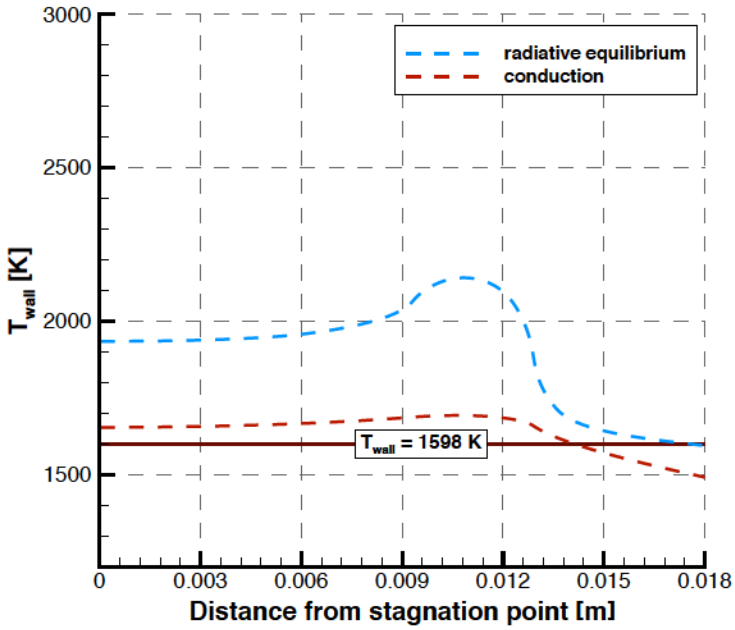

Figure 32: Comparison of wall temperature for different energy balance conditions at the wall.

square root of temperature. When conduction is taken into account, the wall temperature decreases but the nitrogen atom density increases, so no change is observed in the mass removal flux between the two cases.

The comparison between the stagnation point values for these cases along with the experimental data is shown in Table 7. There is an approximately 5% increase in stagnation point heat flux when conduction is included. There is an approximately 17% decrease in stagnation point temperature when conduction into the wall is accounted for. The mass removal rate remains unchanged. The predicted stagnation point heat flux, temperature and mass loss rate for 9.0 kW of deposited power with conductive heat transfer within the sample shows the best agreement with the experimental data. These results show that it is important to include conductive heat transfer within the sample in the energy balance at the wall in such calculations. Overall, these results show that good agreement of computations with all experimental measurements is obtained if all the flow, surface and material physics are included in the simulations.

Table 7: Stagnation point values and mass loss rates for different energy balance conditions at the wall.

	Power $[kW]$	T_{inf} $[K]$	q_{stag} $[W/cm^2]$	$T_{stag}[K]$	Mass loss $[mg/s]$
Radiative equilibrium	9.0	7000	66	1934	0.27
Conduction	9.0	7000	69	1654	0.27
Experiment	13.8	7000	40 - 80	1600	0.2 - 0.6

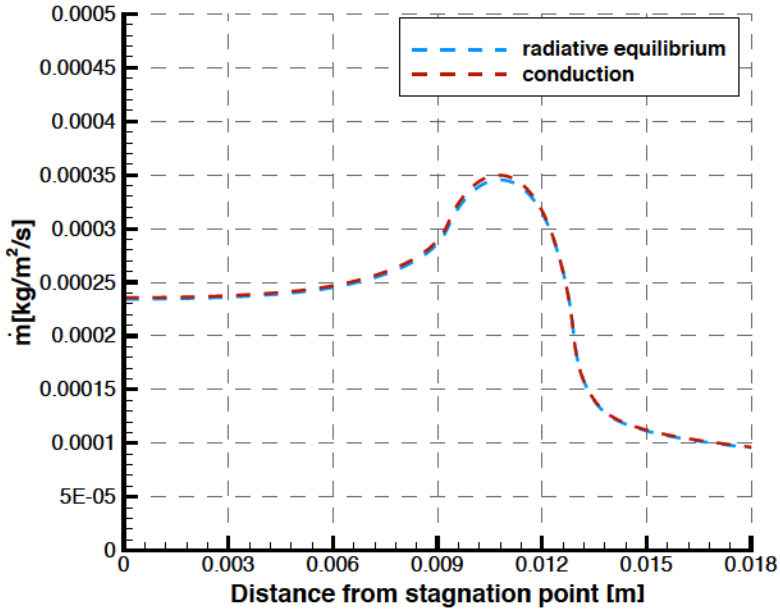

Figure 33: Comparison of mass removal flux for different energy balance conditions at the wall.

4.2 IRV-2 flight trajectory

Results of simulations of the well-documented re-entry trajectory of the IRV-2 vehicle [33, 34] are presented in this Section. IRV-2 is good example of the application of the coupled framework to the simulation of TPS ablation during hypersonic flight.

4.2.1 Numerical Setup

The IRV-2 vehicle is spherical biconic with a nose radius of 0.01905 m and a total length of 1.386 m. The biconic angles are 8.42 and 6.10 degrees, and the change in biconic angle occurs at an axial location of 0.1488 m, measured from the stagnation point. Only the first cone is considered in this study. An image of the IRV-2 vehicle is shown in Figure 34.

The flight conditions that are simulated in this study correspond to the first six points of the trajectory and are listed in Table 8 [33]. Five of these trajectory points include an ablating surface. The freestream composition is assumed to be $Y_{N_2} = 0.7671$ $Y_{O_2} = 0.2329$ at each trajectory point. The gas phase chemistry model is adapted from Ref. [35], and consists of the following twenty species:

$$N_2, O_2, NO, N, O, N_2^+, O_2^+, NO^+, N^+, O^+, e$$
$$CO, CO_2, C_3, CN, C, C_2, NCO, CO^+, C^+$$

The reaction mechanisms and associated Arrhenius rate coefficients for each of the 51 reactions that are included in this model are presented in Ref. [13]. The surface of the vehicle is assumed to be isothermal and at the same temperature as the freestream flow at the first trajectory point. The mesh used to obtain axisymmetric solutions of the flow around the forebody of the vehicle at the first trajectory point contains 96 cells in the axial direction and 88 cells along the body. The mesh provides grid independent solutions at the first trajectory point. The grid is moved with the recessing surface in this study, however the mesh is not adapted to the

Figure 34: The IRV-2 vehicle [33].

flow field at each trajectory point. The error associated with this simplification is expected to be small at the higher altitude trajectory points, but it is expected to increase as the ablation rate, and therefore the vehicle deformation, increases at the lower altitude trajectory points.

The one-dimensional MOPAR material response code is used to model heat conduction into the material, with the material properties of the bulk carbon TPS set to those of generic non-charring carbon [17]. The length of the solid computational domain modeled in MOPAR is 0.01905 m and consists of 101 grid points along each surface line. A zero-gradient boundary condition is enforced at the end of each line.

4.2.2 Surface Chemistry Models

The finite-rate surface chemistry model used to generate baseline results for the IRV-2 vehicle is the Park model [36–38]. The surface reaction mechanisms considered in the Park model are listed in Table 9, along with the parameters used to models those reactions with the FRSC module, which were taken from Ref. [12]. Park's model includes irreversible oxidation of bulk carbon by atomic oxygen and molecular oxygen, as well as irreversible carbon nitridation and reversible carbon sublimation reactions. It is important to note that the lack of reverse reaction pathways for the oxidation and nitridation processes in this model means that it cannot consistently predict an equilibrium state between the gas-phase and the surface at a given surface temperature and pressure.

The use of the Park model to predict recession rates in arc-jet tests of Phenolic Impregnated Carbon Ablator (PICA) has indicated that the reaction efficiency for the carbon nitridation reaction is likely too high, and replacement of the carbon nitridation reaction with reactions modeling the recombination of nitrogen has produced better agreement with experimental data [29]. This modification leads to the second surface chemistry

Table 8: Freestream conditions for the IRV-2 simulations [33].

Trajectory point	Time [s]	Altitude [m]	Velocity [m/s]	Density [kg/m^3]	Temperature [K]
1	0.00	66935	6780.6	1.2505×10^{-4}	227.81
2	4.25	55842	6788.3	5.0454×10^{-4}	258.02
3	6.75	49290	6785.2	1.1344×10^{-3}	270.65
4	8.75	44042	6773.0	2.2593×10^{-3}	261.40
5	10.25	40108	6752.4	3.9957×10^{-3}	250.35
6	11.50	36836	6722.0	6.4268×10^{-3}	241.50

Table 9: Original Park surface chemistry model.

Number	Reaction mechanism	Reaction type	Parameter	E [kJ/mol]
1	O + (s) + C(b) $\rightarrow$ CO + (s)	Eley-Rideal	$\gamma_0 = 0.63$	9.644
2	O_2 + 2(s) + 2C(b) $\rightarrow$ 2CO + 2(s)	Eley-Rideal	$\gamma_0 = 0.50$	0
3	N + (s) + C(b) $\rightarrow$ CN + (s)	Eley-Rideal	$\gamma_0 = 0.30$	0
4	3(s) + 3C(b) $\rightarrow$ C_3 + 3(s)	sublimation	$\gamma_{sub} = 5.19\times10^{13}$	775.81
5	C_3 + 3(s) $\rightarrow$ 3(s) + 3C(b)	Eley-Rideal	$\gamma_0 = 0.10$	0

model that is investigated, shown in Table 10, which is referred to as the modified Park model.

4.2.3 Results

The results obtained using the original Park surface chemistry model shown in Table 9 are discussed first. Figure 35 shows contours of translational temperature in the flow field around the vehicle, as well as streamlines of the flow. The top half of this Figure shows the results predicted at the first trajectory point with ablation, at 4.25 sec during the entry. The bottom half of this Figure shows the results predicted at the last trajectory point investigated in this study, at 11.5 sec during the entry. The shock moves closer to the surface of the vehicle at the later trajectory point. Additionally, the peak temperature reached in the shock layer decreases, as a larger fraction of the molecular O_2 and N_2 in the flow is dissociated at the lower altitude point, which removes energy from the flow. A magnification of the region of the flow field near the stagnation point is also shown in this Figure, which shows that the surface of the TPS has recessed a distance of just under 2 mm at the 11.5 sec trajectory point.

Figure 36 shows contours of the mass fraction of CO in the flow field at the same two trajectory points. The CO produced by surface reactions is confined to the boundary layer over the entire portion of the vehicle

Table 10: Modified Park surface chemistry model.

Number	Reaction mechanism	Reaction type	Parameter	E [kJ/mol]
1	$O + (s) + C(b) \rightarrow CO + (s)$	Eley-Rideal	$\gamma_0 = 0.63$	9.644
2	$O_2 + 2(s) + 2C(b) \rightarrow 2CO + 2(s)$	Eley-Rideal	$\gamma_0 = 0.50$	0
3	$N + (s) \rightarrow N(s)$	Eley-Rideal	$\gamma_0 = 0.05$	0
4	$N + N(s) \rightarrow N_2 + (s)$	Eley-Rideal	$\gamma_0 = 0.05$	0
5	$3(s) + 3C(b) \rightarrow C_3 + 3(s)$	sublimation	$\gamma_{sub} = 5.19 \times 10^{13}$	775.81
6	$C_3 + 3(s) \rightarrow 3(s) + 3C(b)$	Eley-Rideal	$\gamma_0 = 0.10$	0

that is considered, and the boundary layer is thinner at the lower altitude trajectory point as expected. The mass fraction of CO is higher at the lower altitude trajectory point, reaching a peak value of just over 0.3.

Figures 37 and 38 show profiles of predicted surface temperature and mass flux of ablating carbon along the surface of the IRV-2 vehicle for each trajectory point considered in this study. As expected, both the surface temperature and ablating mass flux increase with increasing time of flight. Both the surface temperatures and ablating mass fluxes are significantly higher in the nose region of the vehicle than along the rest of the surface, because the aerothermal environment is the most extreme in this region.

The temperature and ablative mass flux predicted at the stagnation point using the modified Park model is compared to that predicted using the original Park model in Figures 39 and 40. Also shown on these Figures are the results of a previous numerical study that employed an equilibrium surface chemistry model in the form of the B' tables [33], and the results predicted by the ABRES Shape Change Code (ASCC). ASCC is a correlation based code designed for predicting the performance of ablating nose-tips, has been shown to compare very well with flight data for ablating axisymmetric sphere-cones, and has flight data incorporated into its correlations [33]. Figure 39 shows that the original Park chemistry model predicts a lower stagnation point temperature than the previously published results, while the modified Park chemistry models results in better agreement with the previously published values. Figure 40 shows that both the original Park chemistry model and the modified Park chemistry model predict a larger ablating mass flux at each trajectory point investigated than the previously published results. However, the modified Park model predicts a lower ablating mass flux at each trajectory point than the original Park model, in better agreement with previously published results.

Figures 41 and 42 show the predicted production rates of CO, CN, C_3, and N_2 along the surface of the vehicle at the 4.25 s and 10.25 s trajectory points. Note that when the original Park surface chemistry model is used, the production rate of N_2 is zero, as this reaction is not included in that model. Similarly, when the modified Park surface chemistry model is used, there is no production mechanism for CN, and the production rate of CN is therefore zero. Individually, these Figures give an indication of relative importance of each surface reaction included in the Park model. Taken together, they show the increasing role the sublimation reaction plays at the lower altitude trajectory points that correspond to higher surface temperature and pressure.

At the 4.25 s trajectory point, C_3 consumption is predicted around the nose of the vehicle by both chemistry models, however the rate of consumption that is predicted when the modified Park model is used is much lower. This is because, as shown in Figure 39, the surface temperature predicted by that model is higher. The

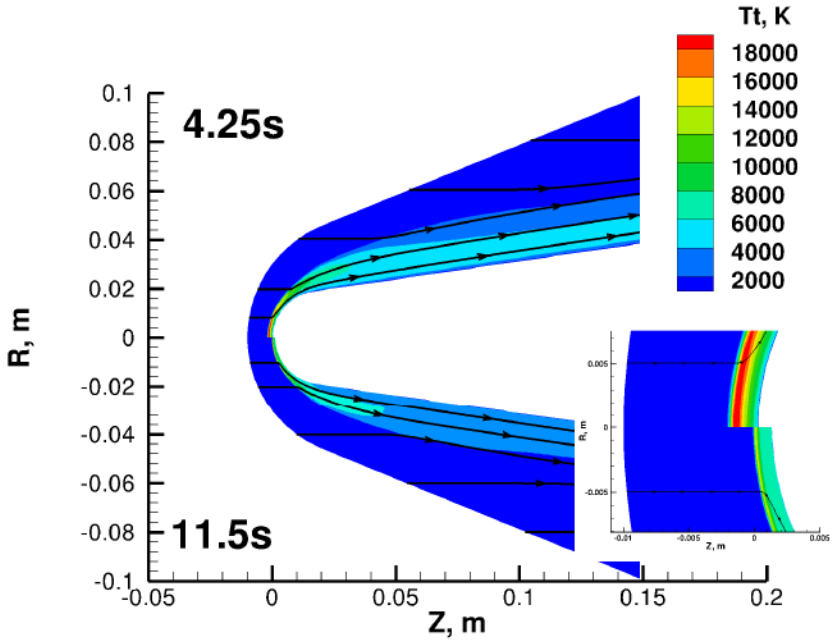

Figure 35: Contours of translational temperature and streamlines at 4.25 sec and 11.5 sec.

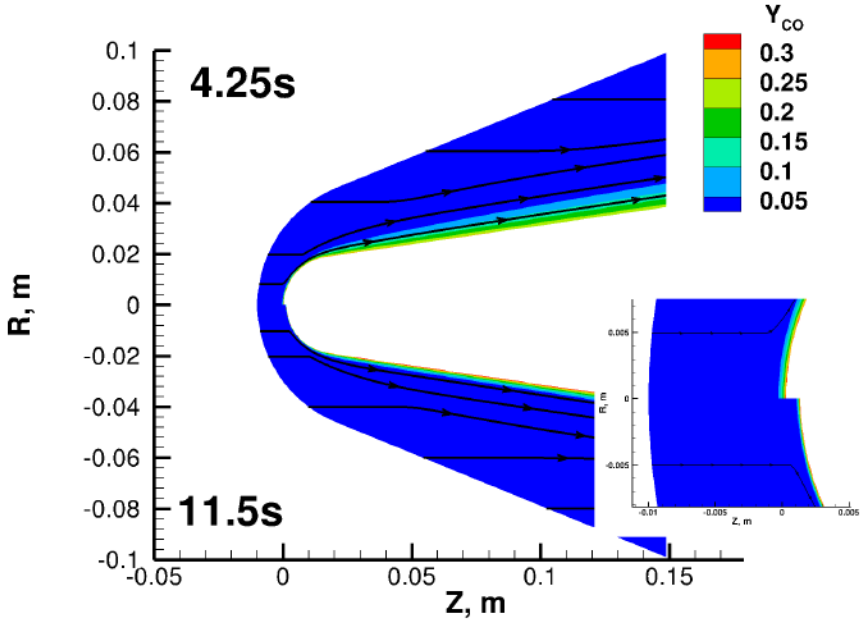

Figure 36: Contours of CO mass fraction at 4.25 sec and 11.5 sec.

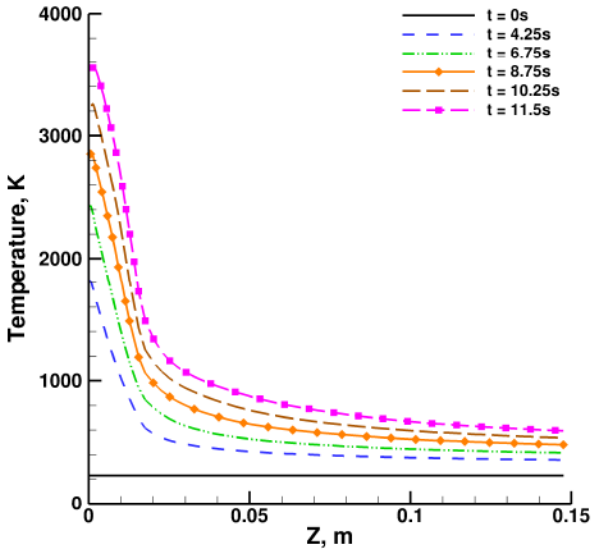

Figure 37: Predicted surface temperature along the length of the vehicle at each trajectory point.

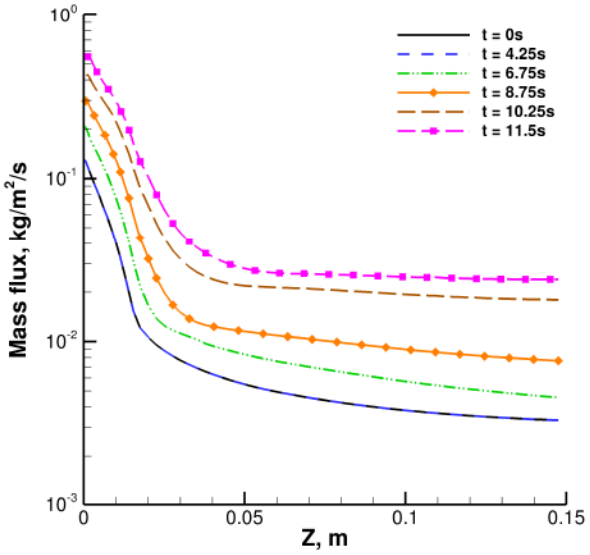

Figure 38: Predicted ablating mass flux along the length of the vehicle at each trajectory point.

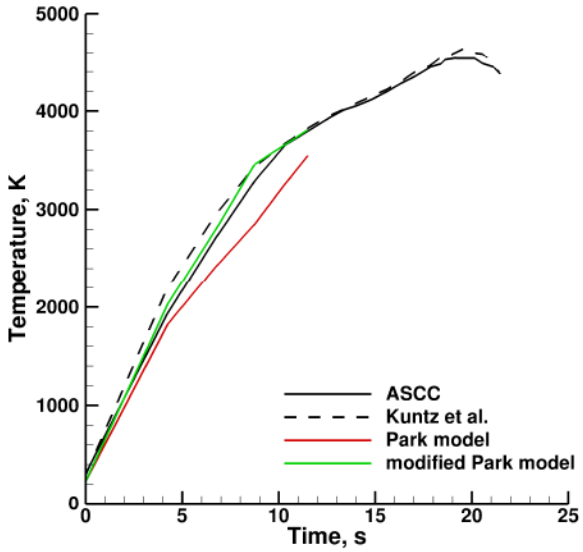

Figure 39: Predicted stagnation point temperature at each trajectory point.

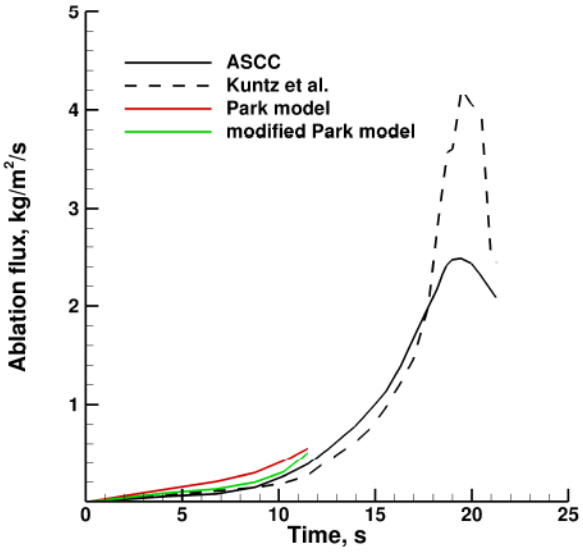

Figure 40: Predicted ablating mass flux at the stagnation point at each trajectory point.

production rates of CO are similar between the two models, with the modified Park model predicting a higher rate of production at the stagnation point. The production rate of CN in the original Park model is much higher than the production rate of N_2 in the modified Park model, which results in a decrease in the consumption of N at the surface when the modified model is used. This also results in a decrease in the mass blowing rate at the surface, which is seen in Figure 40. In general, the magnitudes of the production rates are largest near the nose of the vehicle, and become approximately constant at locations away from the nose of the vehicle.

At the 10.25 s trajectory point, C_3 production has increased, and C_3 is being produced at a similar rate as CO. The modified Park model predicts a larger production rate of C_3, again because the predicted surface temperature is higher. The results obtained using the original Park model show that the CN production rate has increased dramatically relative to the value at the 4.25 s trajectory point, and the CN production rate is still much higher than the N_2 production rate predicted by the modified Park model. This is why the predicted mass ablation rate at the surface is also higher at this trajectory point when original Park model is used, as shown in Figure 40.

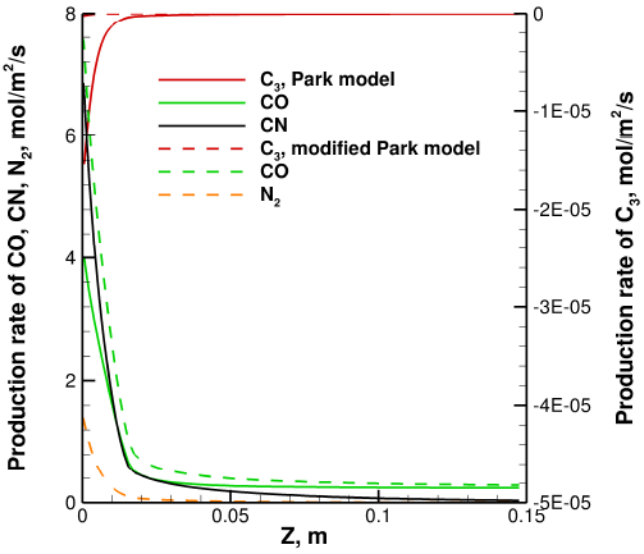

Figure 41: Production rates of CO, CN, C_3, and N_2 along the length of the vehicle at 4.25 s.

These results illustrate the significant effect that the choice of surface chemistry mechanisms and rates can have on the predicted surface properties. The predicted heat fluxes throughout the trajectory and the predicted heat load over the entire trajectory drive the sizing and material choices for a Thermal Protection System. As an example of the differences in the heat flux predictions produced by the two surface chemistry models discussed here, the modified Park model predicts a stagnation point heat flux at the 8.75 sec trajectory point that is approximately 33% higher than that predicted by the original Park model. This difference underscores the need for detailed studies of the air-carbon surface system, in order to increase the fidelity of the surface chemistry models required to perform simulations using this type of coupled computational framework.

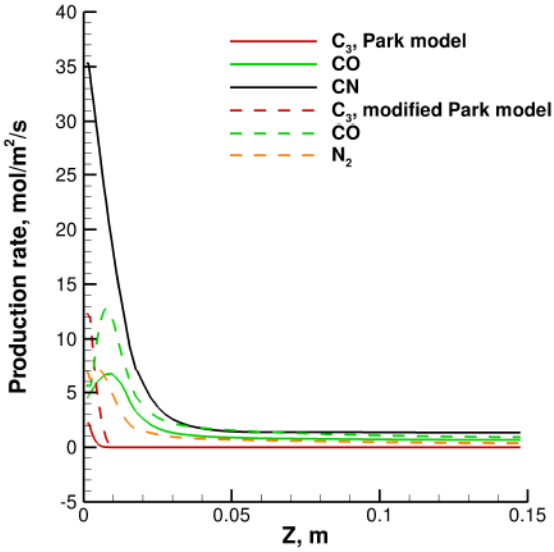

Figure 42: Production rates of CO, CN, C_3, and N_2 along the length of the vehicle at 10.25 s.

5.0 SUMMARY

The details of each of the flow, surface, and material models that form the components of a coupled, computational framework used for simulating the ablation of non-charring materials in a nonequilibrium flow environment, including chemical reactions at the surface that are not in equilibrium, are presented. An approach to coupling the three components, motivated by the large separation of the associated characteristic time scales, is described. Two examples of the use of this coupled framework are discussed in detail.

The application of the coupled framework to modeling the ablation of a graphite sample in an ICP torch facility shows that good agreement of computations with all experimental measurements is obtained only if all the flow, surface and material physics are included in the simulations. Additionally, this example shows that true validation of surface chemistry models requires absolute number density measurements, and that validation of such simulations also requires better characterization of the power absorbed by the plasma in an ICP torch. Lastly, the example shows that it is very important to include the contribution of material response in analyzing the effects of surface chemistry processes. The application of the coupled framework to modeling the ablation of a graphite TPS on a hypersonic vehicle during an Earth re-entry illustrates the need to better characterize the surface reaction mechanisms taking place at a high temperature, air-graphite interface.

ACKNOWLEDGMENTS

The authors gratefully acknowledge Hicham Alkandry (UM) for his assistance with this article, Alexandre Martin (UKy) for his assistance with the MOPAR code, Jon Wiebenga (UM) for his assistance with the MOPAR2 code and with this article, Matthew MacLean (CUBRC) for providing the original FRSC module, and Doug Fletcher (UVM) for providing experimental data. Funding for this work was provided by AFOSR, NASA, and AFRL.

REFERENCES

[1] Johnson, S. M., "Approach to TPS Development for Hypersonic Applications at NASA Ames Research Center," *Proceedings of the 5th European Workshop on Thermal Protection Systems and Hot Structures*, Noordwijk, The Netherlands, 17-19 May 2006.

[2] Edquist, K. T., Dyakonov, A. A., Wright, M. J., and Tang, C. Y., "Aerothermodynamic Environments Definition for the Mars Science Laboratory Entry Capsule," *AIAA Paper 2007-1206*, presented at the 45th AIAA Aerospace Sciences Meeting and Exhibit, Reno, NV, January 2007.

[3] Scalabrin, L. C., *Numerical Simulation of Weakly Ionized Hypersonic Flow Over Reentry Capsules*, Ph.D. thesis, The University of Michigan, 2007.

[4] Martin, A., Scalabrin, L. C., and Boyd, I. D., "High Performance Modeling of Atmospheric Re-entry Vehicles," *Journal of Physics: Conference Series*, Vol. 341, No. 1, 2012, Article 012002.

[5] Wilke, C. R., "A Viscosity Equation for Gas Mixtures," *Journal of Chemical Physics*, Vol. 18, No. 4, 1950, pp. 517–519.

[6] Blottner, F. G., Johnson, M., and Ellis, M., "Chemically Reacting Viscous Flow Program for Multi-Component Gas Mixtures," Technical Report SC-RR-70-754, Sandia Laboratories, Albuquerque, New Mexico, 1971.

[7] Vincenti, W. G. and Kruger, C. H., *Introduction to Physical Gas Dynamics*, Krieger Publishing Company, 1965.

[8] Sutton, K. and Gnoffo, P. A., "Multi-Component Diffusion with Application to Computational Aerothermodynamics," *AIAA Paper 1998-2575*, presented at the 7th AIAA/ASME Joint Thermophysics and Heat Transfer Conference, Albuquerque, NM, June 1998.

[9] MacCormack, R. W. and Candler, G. V., "The Solution of the Navier-Stokes Equations using Gauss-Seidel Line Relaxation," *Computers and Fluids*, Vol. 17, 1989, pp. 135–150.

[10] Karypis, G. and Kumar, V., "METIS: A Software Package for Partitioning Unstructured Graphs, Partitioning Meshes and Computing Fill-Reducing Orderings of Sparse Matrices," Tech. rep., University of Minnesota, 1998.

[11] Marschall, J. and MacLean, M., "Finite-Rate Surface Chemistry Model, I: Formulation and Reaction System Examples," *AIAA-2011-3783*, presented at the 42nd AIAA Thermophysics Conference, Honolulu, HI, June 2011.

[12] Marschall, J. and MacLean, M., "Finite-Rate Surface Chemistry Model, II: Coupling to Viscous Navier-Stokes Code," *AIAA-2011-3784*, presented at the 42nd AIAA Thermophysics Conference, Honolulu, HI, June 2011.

[13] Alkandry, H., Farbar, E. D., and Boyd, I. D., "Evaluation of Finite-Rate Surface Chemistry Models for Simulation of the Stardust Reentry Capsule," *AIAA Paper 2012-2874*, presented at the 43rd AIAA Thermophysics Conference, New Orleans, LA, June 2012.

[14] McBride, B. J., Zehe, M. J., and Gordon, S., "NASA Glenn Coefficients for Calculating Thermodynamic Properties of Individual Species," NASA/TP-2002-211556, National Aeronautics and Space Administration, September 2002.

[15] Martin, A. and Boyd, I. D., "Strongly Coupled Computation of Material Response and Nonequilibrium Flow for Hypersonic Ablation," *AIAA-2009-3597*, presented at the 41st AIAA Thermophysics Conference, San Antonio, TX, June 2009.

[16] Martin, A. and Boyd, I. D., "Simulation of Pyrolysis Gas within a Thermal Protection System," *AIAA-2008-3805*, presented at the 40th AIAA Thermophysics Conference, Seattle, Washington, June 2008.

[17] Amar, A. J., *Modeling of One-Dimensional Ablation with Porous Flow using Finite Control Volume Prodedure*, Master's thesis, North Carolina State University, Raleigh, NC, 2006.

[18] Blackwell, B. and Hogan, R., "Numerical Solution of Axisymmetric Heat Conduction Problems Using Finite Control Volume Technique," *Journal of Thermophysics and Heat Transfer*, Vol. 7, No. 3, 1993, pp. 462–471.

[19] Wiebenga, J. E. and Boyd, I. D., "Computation of Multi-dimensional Material Response Coupled to Hypersonic Flow," *AIAA-2012-2873*, presented at the 43rd AIAA Thermophysics Conference, New Orleans, Louisiana, June 2012.

[20] Wiebenga, J. E. and Boyd, I. D., "Manufactured Solutions for Verification of a Coupled Flow and Material Response Code," *AIAA-2013-2646*, presented at the 44th AIAA Thermophysics Conference, San Diego, CA, June 2013.

[21] Lutz, A., Owens, W., Meyers, J., Fletcher, D., and Marschall, J., "Investigation of CN Production from Carbon Materials in Nitrogen Plasmas," *AIAA Paper 2011-901*, January 2011.

[22] Owens, W. P., Uhl, J., Dougherty, M., Lutz, A., Meyers, J., and Fletcher, D. G., "Development of a 30kW Inductively Coupled Plasma Torch for Aerospace Material Testing," *AIAA Paper 2010-4322*, June 2010.

[23] Kolesnikov, A. F., "Extrapolation from High Enthalpy Tests to Flight Based on the Concept of Local Heat Transfer Simulation," NATO RTO EN-8, Neuilly-sur-Seine Cedex, France, 1999, pp. 8B/1–14.

[24] Sheppard, R. G., Mathes, D. M., and Bray, D. J., *Properties and Characteristics of Graphite*, Poco Graphite, Inc., November 2001.

[25] McBride, B. J. and Gordon, S., "Chemical Equilibrium with Applications (CEA)," [http://www.grc.nasa.gov/WWW/CEAWeb/], accessed in 2011.

[26] Lutz, A., Meyers, J., Owens, W., Smith, S., and Fletcher, D. G., "Experimental Analysis of Carbon Nitridation and Oxidation Efficiency with Laser-Induced Fluorescence," *51st AIAA Aerospace Sciences Meeting*, No. AIAA 2013-0924, Grapevine, Texas, 07-10 January 2013.

[27] Anna, A., *Numerical Modeling of Surface Chemistry Processes for Hypersonic Entry Environments*, Ph.D. thesis, University of Michigan, 2013.

[28] Gordeev, A. N., Kolesnikov, A. F., and Yakushin, M. I., "Effect of Surface Catalytic Activity on Nonequilibrium Heat Transfer in a Subsonic Jet of Dissociated Nitrogen," *Fluid Dynamics*, Vol. 20, 1985, pp. 478–484.

[29] Driver, D. M. and MacLean, M., "Improved Predictions of PICA Recession in Arc Jet Shear Tests," *AIAA Paper 2011-0141*, presented at the 49th AIAA Aerosciences Meeting, Orlando, FL, January 2011.

[30] Anna, A., Boyd, I. D., Colombo, V., Ghedini, E., Sanibondi, P., Boselli, M., and Gherardi, M., "Computational Modeling of Surface Catalysis for Graphite Exposed to High-enthalpy Nitrogen Flow," *RTO-AVT-199*, January 2012.

[31] Owens, W., *personal communication*, Mechanical Engineering, University of Vermont, Burlington,VT.

[32] Lutz, A. J., *personal communication*, Mechanical Engineering, University of Vermont, Burlington,VT.

[33] Kuntz, D. W., Hassan, B., and Potter, D. L., "Predictions of Ablating Hypersonic Vehicles Using an Iterative Coupled Fluid/Thermal Approach," *Journal of Thermophysics and Heat Transfer*, Vol. 15, No. 2, 2001, pp. 129–139.

[34] Thompson, R. A. and Gnoffo, P. A., "Implementation of a Blowing Boundary Condition in the LAURA Code," *AIAA Paper 2008-1243*, 2008, pp. 2369–2377.

[35] Martin, A., Boyd, I. D., Cozmuta, I., and Wright, M. J., "Chemistry Model for Ablating Carbon-Phenolic Material During Atmospheric Re-entry," *AIAA-2010-1175*, presented at the 48th AIAA Aerospace Sciences Meeting and Exhibit, Orlando, FL, Jan. 2010.

[36] Park, C. and Ahn, H., "Stagnation-Point Heat Transfer Rates for Pioneer-Venus Probes," *Journal of Thermophysics and Heat Transfer*, Vol. 13, No. 1, 1999, pp. 33–41.

[37] Chen, Y.-K. and Milos, F. S., "Navier-Stokes Solutions with Finite Rate Ablation for Planetary Mission Earth Reentries," *Journal of Spacecraft and Rockets*, Vol. 42, No. 6, 2005, pp. 961–970.

[38] Park, C., "Stagnation-Point Ablation of Carbonaceous Flat Disks - Part I: Theory," *AIAA Journal*, Vol. 21, No. 11, 1983, pp. 1588–1594.